Direct numerical simulation of the turbulent kinetic energy and energy dissipation rate in a cylinder wake

Hongyi Jiang[1], Xiaoyuan Hu[2], Liang Cheng[1,2†], and Tongming Zhou[1]

[1]School of Engineering, The University of Western Australia, 35 Stirling Highway, Perth, WA 6009, Australia

[2]School of Marine Science and Engineering, Guangzhou International Campus, South China University of Technology, Guangzhou, 511442, PR China

Abstract

The turbulent kinetic energy and energy dissipation rate in the wake of a circular cylinder are examined at a Reynolds number (*Re*) of 1000. The turbulence characteristics are quantified using direct numerical simulation, which provides a comprehensive dataset that is almost impossible to acquire from physical experiments. The energy dissipation rate is decomposed into the components due to the mean flow, the coherent primary vortices and the remainder. It is found that the remainder component, which develops only in a three-dimensional turbulent wake and resides mainly in the regions of vortices, accounts for 95% and 97% of the total dissipation rate for 10 and 20 cylinder diameters downstream of the cylinder, respectively (while the remainder accounts for 62% and 83% of the total turbulent kinetic energy). Based on the remainder component, the validity of local isotropy, local axisymmetry, local homogeneity and homogeneity in the *y*-*z* plane for the turbulent dissipation in the wake is examined. The analysis reveals that the turbulent dissipation is largely locally homogeneous, but not locally isotropic or axisymmetric, even after the annihilation of the primary vortex street. In addition, the performances of the four corresponding surrogates to the true dissipation rate are evaluated. Owing to the general validity of local homogeneity, the surrogates of local homogeneity and homogeneity in the *y*-*z* plane perform well. Although local axisymmetry does not hold, the corresponding surrogate performs well, because errors from different terms largely cancel out. However, the surrogate of local isotropy generally underestimates the true dissipation rate.

1. Introduction

The canonical case of steady approaching flow past a smooth and slender circular cylinder (referred to as flow past a circular cylinder hereafter) has been a classical topic in fluid mechanics owing to its physical complexity and extensive engineering applications. The sole governing parameter of the flow is the Reynolds number *Re* (=

†Correspondence author: liang.cheng@uwa.edu.au

UD/ν), which is defined based on the velocity of the approaching flow (U), the diameter of the cylinder (D), and the kinematic viscosity of the fluid (ν). Despite its geometric simplicity, complex evolutions of the flow with increasing Re have been discovered, e.g. flow separation, vortex shedding, three-dimensional (3D) wake transition, and transition to turbulence in the wake, the separating shear layer and the boundary layer (see e.g. Williamson, 1996; Zdravkovich, 1997). Fig. 1 illustrates an instantaneous 3D turbulent wake structure at Re = 1000, where the spanwise vorticity (ω_z) and streamwise vorticity (ω_x) are defined in a non-dimensional form:

$$\omega_z = \left(\frac{\partial v}{\partial x} - \frac{\partial u}{\partial y} \right) \frac{D}{U}, \tag{1.1}$$

$$\omega_x = \left(\frac{\partial w}{\partial y} - \frac{\partial v}{\partial z} \right) \frac{D}{U}, \tag{1.2}$$

where (x, y, z) and (u, v, w) are the Cartesian coordinates and velocity components in the streamwise, transverse (cross-flow) and spanwise directions, respectively.

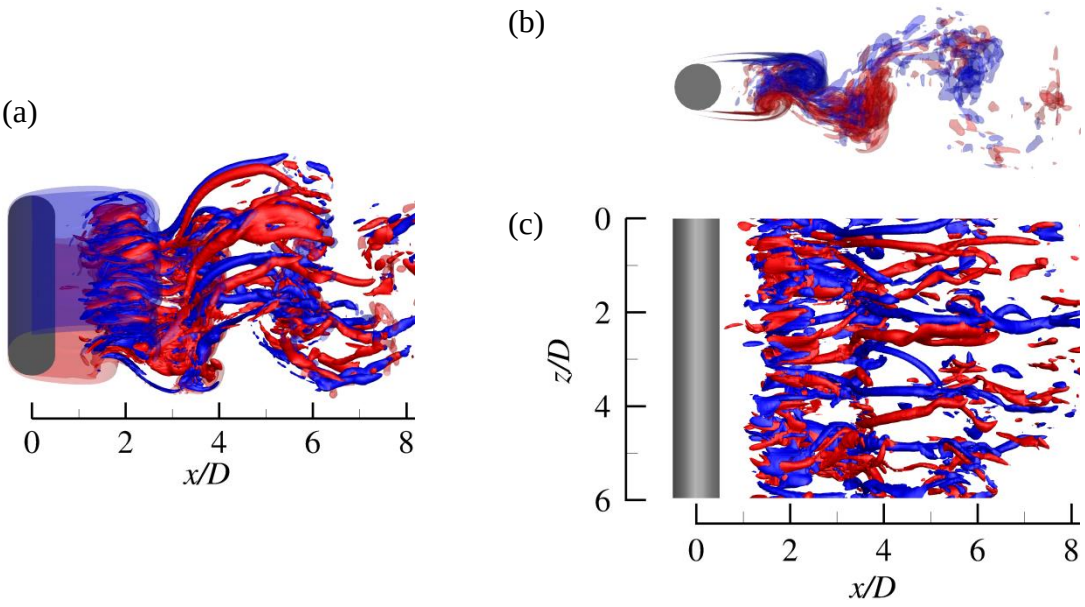

Fig. 1. Instantaneous vorticity field in the turbulent wake of a circular cylinder at Re = 1000: (a) iso-surfaces of spanwise (translucent) and streamwise (opaque) vortices, (b) iso-surfaces of spanwise vortices only, and (c) iso-surfaces of streamwise vortices only. Red and blue represent positive and negative vorticity values of ±4, respectively. The flow is from left to right past the cylinder on the left.

The above-mentioned flow characteristics are generally observed close to the cylinder. An exception is the turbulent wake observed at $Re \gtrsim 260$ (Williamson, 1996), which develops into the far-wake region. Not surprisingly, the turbulent intermediate and far wake have been far less studied in the literature than other flow characteristics, which is likely due to the difficulty in measuring the turbulent quantities accurately by physical experiments, and the high computational cost associated with resolving the

intermediate and far wake in 3D numerical simulations.

In addition to the more well-known quantity of turbulent kinetic energy, another major quantity governing the turbulent wake is the kinetic energy dissipation rate, which was examined by several experimental studies in the literature (e.g. Browne et al., 1987; George and Hussein, 1991; Zhou et al., 2003; Ducci et al., 2005; Chen et al., 2018). For the turbulent wake, the velocity and the kinetic energy dissipation rate can be decomposed into three components, i.e. a mean (time-averaged) component, a coherent fluctuation component associated with the primary vortices, and a remainder associated with the smaller-scale structures (Reynolds and Hussain, 1972; Cantwell and Coles, 1983; Elsner and Elsner, 1996). The remainder consists of two parts, i.e. an incoherent fluctuation associated with the random turbulence, and a coherent fluctuation associated with the rib-like mode B streamwise vortices (Williamson, 1996; Zhang et al., 2000) which are randomly distributed along the spanwise direction (Fig. 1c). For an instantaneous flow quantity s (e.g. a velocity component), the three components are denoted s_m, $\tilde{s}$ and s_r, respectively, and the total fluctuation is denoted s', i.e.

$$s = s_m + \tilde{s} + s_r = s_m + s' . \tag{1.3}$$

Based on the assumption that the two fluctuation components $\tilde{s}$ and s_r are uncorrelated (Reynolds and Hussain, 1972), the total kinetic energy dissipation rate ε can be decomposed into the contributions from the mean flow, the coherent primary vortices and the remainder, i.e. (Elsner and Elsner, 1996)

$$\varepsilon = \varepsilon_m + \tilde{\varepsilon} + \varepsilon_r = \varepsilon_m + \varepsilon' , \tag{1.4}$$

where

$$\varepsilon = \nu \overline{\frac{\partial u_i}{\partial x_j}\left(\frac{\partial u_i}{\partial x_j} + \frac{\partial u_j}{\partial x_i} \right)}, \tag{1.5}$$

$$\varepsilon_m = \nu \frac{\partial u_{m,i}}{\partial x_j}\left(\frac{\partial u_{m,i}}{\partial x_j} + \frac{\partial u_{m,j}}{\partial x_i} \right), \tag{1.6}$$

$$\tilde{\varepsilon} = \nu \overline{\frac{\partial \tilde{u}_i}{\partial x_j}\left(\frac{\partial \tilde{u}_i}{\partial x_j} + \frac{\partial \tilde{u}_j}{\partial x_i} \right)}, \tag{1.7}$$

$$\varepsilon_r = \nu \overline{\frac{\partial u_{i,r}}{\partial x_j}\left(\frac{\partial u_{i,r}}{\partial x_j} + \frac{\partial u_{j,r}}{\partial x_i} \right)}, \tag{1.8}$$

$$\varepsilon' = \nu \overline{\frac{\partial u_i'}{\partial x_j}\left(\frac{\partial u_i'}{\partial x_j} + \frac{\partial u_j'}{\partial x_i} \right)}, \tag{1.9}$$

where an overbar denotes a mean value (and ε_m is a mean value by definition), u_i is the velocity component in the direction x_i, and i = 1, 2 and 3 represent the streamwise, transverse and spanwise directions, respectively. In Appendix A, a numerical validation of the relationship $\varepsilon = \varepsilon_m + \tilde{\varepsilon} + \varepsilon_r$ is reported based on the present

numerical results.

By decomposing ε' into $\tilde{\varepsilon}$ and ε_r, Chen et al. (2018) quantified the transverse distribution of coherent contribution $\tilde{\varepsilon}/\left(\tilde{\varepsilon}+\varepsilon_r\right)$ at x/D = 10, 20 and 40 of the turbulent wake at Re = 2500. They showed that the maximum coherent contribution at x/D = 10 was ~ 9% (at y/D = 0.6), while the maximum coherent contribution at x/D = 20 was ~ 4% (at y/D = 0.2). Similarly, Ducci et al. (2005) examined the turbulent wake at Re = 6700 and 7200, and found that at x/D = 10 the coherent component accounted for 10%–15% of the total dissipation rate.

The minor coherent contribution at x/D > 20 (Chen et al., 2018) may explain why other experimental studies, which focused mainly on the relatively far wake, did not quantify $\tilde{\varepsilon}$ and ε_r and instead used ε' directly. Indeed, the focus of most of the experimental studies was on an appropriate approximation of the dissipation rate using simplified surrogates, since it was extremely difficult to measure all twelve velocity derivative terms constituting the dissipation rate in physical experiments (Browne et al., 1987; Chen et al., 2018). As summarised by Chen et al. (2018), commonly-used surrogates include local isotropy (Taylor, 1935), local axisymmetry with respect to the streamwise direction x (George and Hussein, 1991), local homogeneity (Taylor, 1935), and homogeneity in the y-z plane (Zhu and Antonia, 1997). The four surrogates are expressed as follows, where (u_1, u_2, u_3) and (x_1, x_2, x_3) are used interchangeably with (u, v, w) and (x, y, z), respectively.

$$\varepsilon'_{iso} = 15\nu\overline{\left(\frac{\partial u'}{\partial x}\right)^2}, \tag{1.10}$$

$$\varepsilon'_{axis} = \nu\left[\frac{5}{3}\overline{\left(\frac{\partial u'}{\partial x}\right)^2} + 2\overline{\left(\frac{\partial u'}{\partial z}\right)^2} + 2\overline{\left(\frac{\partial v'}{\partial x}\right)^2} + \frac{8}{3}\overline{\left(\frac{\partial v'}{\partial z}\right)^2}\right], \tag{1.11}$$

$$\varepsilon'_{hom} = \nu\overline{\frac{\partial u'_i}{\partial x_j}\frac{\partial u'_i}{\partial x_j}}, \tag{1.12}$$

$$\varepsilon'_{yz} = \nu\left[4\overline{\left(\frac{\partial u'}{\partial x}\right)^2} + \overline{\left(\frac{\partial u'}{\partial y}\right)^2} + \overline{\left(\frac{\partial u'}{\partial z}\right)^2} + \overline{\left(\frac{\partial v'}{\partial x}\right)^2} + \overline{\left(\frac{\partial v'}{\partial z}\right)^2} + \overline{\left(\frac{\partial w'}{\partial x}\right)^2} + \overline{\left(\frac{\partial w'}{\partial y}\right)^2} + 2\overline{\left(\frac{\partial u'}{\partial y}\right)\left(\frac{\partial v'}{\partial x}\right)} + 2\overline{\left(\frac{\partial u'}{\partial z}\right)\left(\frac{\partial w'}{\partial x}\right)} - 2\overline{\left(\frac{\partial v'}{\partial z}\right)\left(\frac{\partial w'}{\partial y}\right)}\right], \tag{1.13}$$

Not surprisingly, the surrogate of local isotropy, which requires the measurement of only one of the twelve terms, is often reported to be inaccurate (e.g. Browne et al., 1987; George and Hussein, 1991). On the other hand, it is difficult to evaluate the accuracy of the other three surrogates, because the true value ε' is almost impossible to be measured from physical experiments (which involves the use of highly complex hot-wire probes or 3D particle image velocimetry (PIV) techniques, albeit still limited by spatial and temporal resolutions). Even for the velocity gradients which are measurable by the experiments, moderate errors may arise from e.g. limited spatial

resolution of the probes for measuring the velocity gradients and the use of Taylor's hypothesis (Zhou et al., 2003). For example, Zhou et al. (2003) and Chen et al. (2018) stated that in their experiments the velocity gradients were underestimated by approximately 18%–7% at x/D = 10–40.

To overcome the experimental limitations, direct numerical simulations (DNS) are used in the present study to quantify the full energy dissipation rate ε' and its surrogates and to evaluate their adequacy in representing ε'. Chen et al. (2018) also commented on the lack of numerical datasets for evaluating the true value of ε', which justifies the necessity of the present study. The present DNS results provide guidance and support to experimental studies on the use of appropriate surrogates for ε'. The present study also examines whether the turbulent wake is indeed locally isotropic, axisymmetric and homogeneous.

2. Numerical model

2.1. Numerical method

The governing equations for flow past a circular cylinder are the continuity and incompressible Navier–Stokes equations:

$$\frac{\partial u_i}{\partial x_i} = 0, \tag{2.1}$$

$$\frac{\partial u_i}{\partial t} + u_j \frac{\partial u_i}{\partial x_j} = -\frac{\partial p}{\partial x_i} + \nu \frac{\partial^2 u_i}{\partial x_j \partial x_j}. \tag{2.2}$$

where t is time and p is kinematic pressure (pressure divided by fluid density).

The governing equations were solved by the open-source code Nektar++ (Cantwell et al., 2015) through the so-called quasi-3D approach. Specifically, the flow in the x-y plane was solved by a high-order spectral/*hp* element method (Karniadakis and Sherwin, 2005), while that in the spanwise direction was represented by a Fourier expansion (Karniadakis, 1990). This approach provided a higher computational efficiency than conventional finite element and similar methods (Cantwell et al., 2015; Moxey et al., 2020). The numerical simulations adopted the unsteady Navier–Stokes solver embedded in Nektar++, together with the velocity correction scheme (Karniadakis et al., 1991), a second-order implicit–explicit (IMEX) time-integration scheme and a continuous Galerkin projection. The spectral vanishing viscosity (SVV) technique proposed by Kirby and Sherwin (2006) was used to stabilise the solution. The SVV cut-off ratio was set to 0.9 (with 1.0 being no effect on the simulation), while the SVV diffusion coefficient was set to 0.1 (with 0 being no effect).

2.2. Computational domain and mesh

The present study investigated mainly the turbulent wake at Re = 1000. A rectangular computational domain was adopted for the x-y plane. The centre of the cylinder was

placed at (x, y) = (0, 0). The computational domain size was $-30 \leq x/D \leq 120$ in the streamwise direction and $-30 \leq y/D \leq 30$ in the transverse direction.

Fig. 2 shows the macro-element mesh near the cylinder. The perimeter of the cylinder was discretised equally with 48 macro-elements. The first layer of macro-elements had a radial size of 0.00553D. To resolve the wake characteristics, the streamwise size of the macro-elements for x/D = 4 – 120 was fixed at 0.2D. The total number of macro-elements in the x-y plane was 26,922. Each macro-element contained a further quadrilateral expansion using 4th-order Lagrange polynomials (denoted N_p = 4).

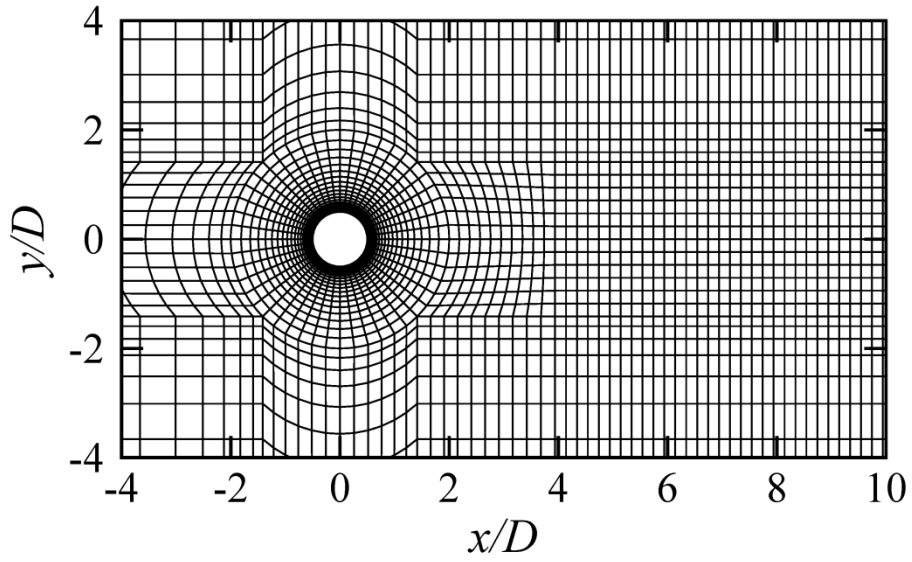

Fig. 2. The macro-element mesh near the cylinder.

The 3D mesh was constructed by using 128 Fourier planes over the spanwise domain length L_z/D = 6. The adequacy of L_z/D = 6 was demonstrated by Jiang and Cheng (2017) based on a comparison of L_z/D = 6 and 12 at Re = 1000. The adequacy of 128 Fourier planes for L_z/D = 6 was demonstrated by Jiang and Cheng (2021) at Re = 3900 and was expected to be applicable to Re = 1000.

The boundary conditions for the computational domain were specified as follows. At the inlet (x/D = –30) and transverse (y/D = ±30) boundaries, a uniform velocity (u, v, w) = (U, 0, 0) was specified, together with a high-order Neumann condition for the pressure (Karniadakis et al., 1991). At the outlet (x/D = 120) boundary, the velocity was set to the Neumann condition, while the pressure was specified as a reference value of zero. At the cylinder surface, the no-slip condition was used. At the two boundaries perpendicular to the spanwise direction, periodic boundary conditions were applied.

At the beginning of the simulation, the internal flow followed an impulsive start. The non-dimensional time-step size ($\Delta t^* = \Delta tU/D$) was 0.003125, which corresponded to a Courant–Friedrichs–Lewy (CFL) limit of 0.53. Each case was simulated for at least 1000 non-dimensional time units (defined as $t^* = tU/D$), with the first 400 time units used to phase out the transients and the remainder for the

statistics and analysis. The numerical simulations were conducted on a Cray XC40 system supercomputer. For the reference case with N_p = 4, the computational cost for 1000 time units was approximately 82,200 core hours (a parallel computation using 120 processors and approximately 685 hours of wall-clock time for each processor).

Appendix B reports a detailed mesh convergence study, which includes separate examinations of the effects of overall mesh resolution, element stretching in the wake region, statistical time period, sample interval, the SVV technique and the time integration technique on the prediction of the mean kinetic energy dissipation rate ε. The reference case examined in Appendix B employed the mesh shown in Fig. 2 (with N_p = 4 and no element stretching along the wake), a statistical time period of 100T (T being the vortex shedding period), a sample interval of T/16 (i.e. a total of 1600 fields over the statistical time period of 100T), and a non-dimensional time-step size of 0.003125. Based on Appendix B, the reference case was deemed adequate for the present study. Nevertheless, for the main body of the present study the ε value (and the corresponding velocity derivative terms) was obtained with a doubled statistical time period of 200T (i.e. a total of 3200 fields), because the data were readily available from the mesh convergence study. In addition to the time average, the results were also averaged along the spanwise direction and between the two sides of the wake centreline.

2.3. Phase-averaging technique

A reliable phase-averaging technique is needed to extract the coherent structures. The present phase-averaging technique generally follows that used by e.g. Matsumura and Antonia (1993), Zhou et al. (2002) and Chen et al. (2018) for wind-tunnel experimental results. However, some modifications of the technique are made to facilitate processing of the present numerical results, because the present numerical data consist of the output of a large number of instantaneous flow fields, whereas wind-tunnel data are generally sampled at selected discrete points.

To extract the coherent structures at a specific streamwise location in the wake, the time history of the transverse velocity v sampled at this streamwise location and y/D = 1 is used as a reference signal. To maximise the length of statistical data, the reference signals are taken at four equally-spaced spanwise locations (i.e. z/D = 0, 1.5, 3 and 4.5) and are processed individually. Each v signal is filtered using a fourth-order Butterworth filter with the centre frequency set at the primary vortex shedding frequency (e.g. Zhou et al., 2002; Chen et al., 2018), as identified from the FFT of the signal. Fig. 3(a) illustrates the v signal sampled at (x/D, y/D, z/D) = (10, 1, 3) and the corresponding filtered signal. Based on the filtered signal, the local peaks in the time history are set to phase φ = 0, while the local troughs are set to phase $\varphi = \pi$. Between each peak and trough, the time range is equally divided into 8 intervals, such that a period from a peak to the next peak is divided into 16 intervals. From a peak to the next peak, the selected phases are set to $\varphi = n \times (2\pi/16)$, where n is an integer from 0 to 16. The instantaneous flow fields at the selected phases are then used for the phase average. The phase average (denoted by $\langle \cdot \rangle$) of a flow field $\boldsymbol{u}$ at a specific phase

(denoted by the subscript p) is calculated as

$$\langle \boldsymbol{u} \rangle_p = \frac{1}{N_p} \sum_{i=1}^{N_p} \boldsymbol{u}_{p,i} , \tag{2.3}$$

where N_p is the number of periods for the phase average. Finally, the phase-averaged flow fields obtained individually at each of the four spanwise locations are further averaged to obtain the final phase-averaged flow field. For the final phase-averaged flow field, only the area near the streamwise location where the v signals are sampled is meaningful.

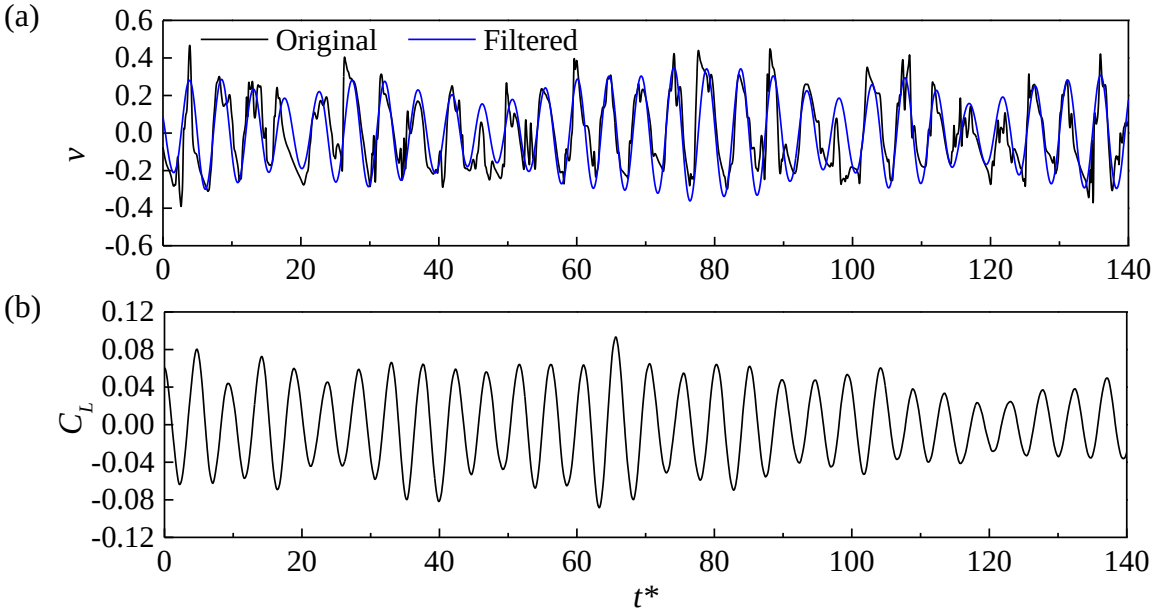

Fig. 3. Reference signals for the phase average: (a) the v signal sampled at (x/D, y/D, z/D) = (10, 1, 3), and (b) the time history of C_L. To facilitate comparison between the original and filtered signals in panel (a), the filtered results are multiplied by 5.246, such that the standard deviation of the two signals is the same, while the phase is unchanged.

Similarly, the time history of the lift coefficient (C_L) on the cylinder can be used as a reference signal for a phase average to extract the coherent structures near x/D = 0. Since the C_L signal varies smoothly over time (Fig. 3b), no filter is used. For this phase-averaged flow field, only the area near x/D = 0 is meaningful.

At a specific phase p, the coherent component of the velocity field ($\tilde{\boldsymbol{u}}_p$) is determined based on the final phase-averaged velocity field ($\langle \boldsymbol{u} \rangle_p$) and the time- and span-averaged velocity field ($\boldsymbol{u}_m$), i.e.

$$\tilde{\boldsymbol{u}}_p = \langle \boldsymbol{u} \rangle_p - \boldsymbol{u}_m , \tag{2.4}$$

The coherent component of the dissipation rate at phase p ($\tilde{\varepsilon}_p$) is calculated by

substituting $\tilde{\boldsymbol{u}}_p$ into equation (1.7). Finally, the averaged coherent contribution of the dissipation rate ($\tilde{\varepsilon}$) is determined as an average of the $\tilde{\varepsilon}_p$ values over the 16 selected phases over the vortex shedding period. This approach is similar to the "structural averaging" technique used by e.g. Zhou et al. (2002) and Chen et al. (2018) for experimental datasets.

3. Numerical results

3.1. Pattern of the primary vortex street

Following the phase-averaging technique introduced in section 2.3, it is interesting to examine the differences of the phase-averaged flow fields obtained based on the reference signals sampled at different x/D. This comparison sheds light on how well a phase-averaged flow field obtained based on the reference signal at a specific x/D represents the flow over a range of x/D. For example, the C_L signal was commonly used in previous numerical and PIV experimental studies in obtaining the phase-averaged flow field, and it is unclear to what extent this phase-averaged flow field represented the actual wake pattern over a range of x/D.

Fig. 4 shows the phase-averaged spanwise vorticity fields in the turbulent wake of Re = 1000, determined based on the C_L signal (Fig. 4a) and the v signals sampled at x/D = 10 (Fig. 4b) and x/D = 20 (Fig. 4c). The vorticity fields are shown at a phase where the reference signal reaches its maximum. Qualitatively, the three vorticity fields show similar patterns, where the primary vortex street gradually decays with distance downstream. The decay of the primary vortex street for the three cases shown in Fig. 4(a–c) is quantified by the streamwise variation of the peak vorticity of vortices in Fig. 5(a–c), respectively. The fitted curves in Fig. 5(a–c) are further summarised in Fig. 5(d). As expected, the C_L signal gives rise to the largest peak vorticity very close to the cylinder, while the v signals sampled at x/D = 10 and 20 yield the largest peak vorticity at x/D = 10 and 20, respectively (highlighted by the open circles in Fig. 5(d)). Based on the C_L signal, the peak vorticity values at x/D = 10 and 20 are under-predicted by 20% and 27%, respectively. Based on the v signal sampled at x/D = 10, the peak vorticity at x/D = 20 is under-predicted by a smaller extent of 8%. Based on the v signal sampled at x/D = 20, the peak vorticity at x/D = 10 is under-predicted by 44%. Therefore, the quantitative validity of a phase-averaged flow field is well within 10D of the streamwise location for the reference signal (especially when extending upstream).

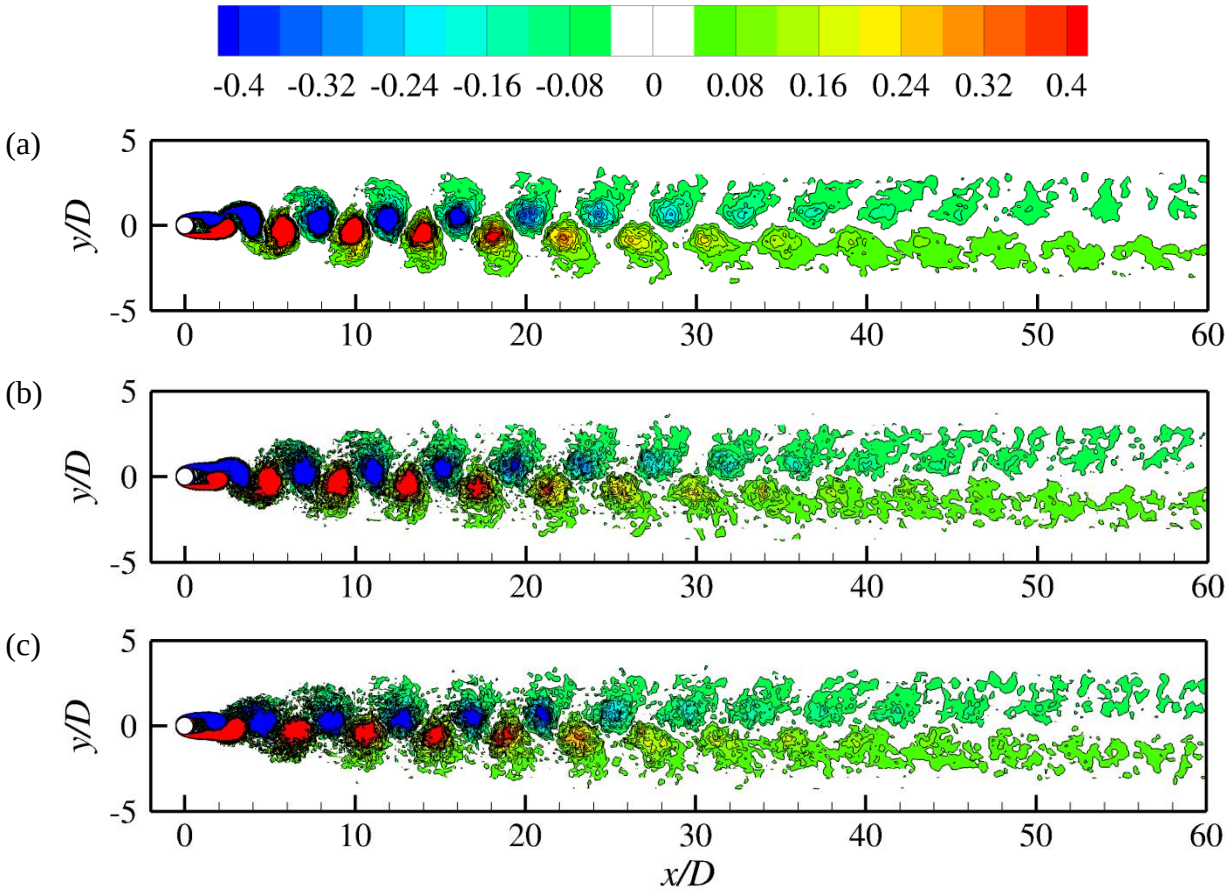

Fig. 4. Phase-averaged spanwise vorticity field in the turbulent wake of *Re* = 1000, determined based on the reference signal of (a) the lift coefficient (i.e. at *x*/*D* ~ 0), (b) transverse velocity *v* sampled at *x*/*D* = 10, and (c) transverse velocity *v* sampled at *x*/*D* = 20. All the vorticity fields are shown at a phase where the reference signal reaches its maximum.

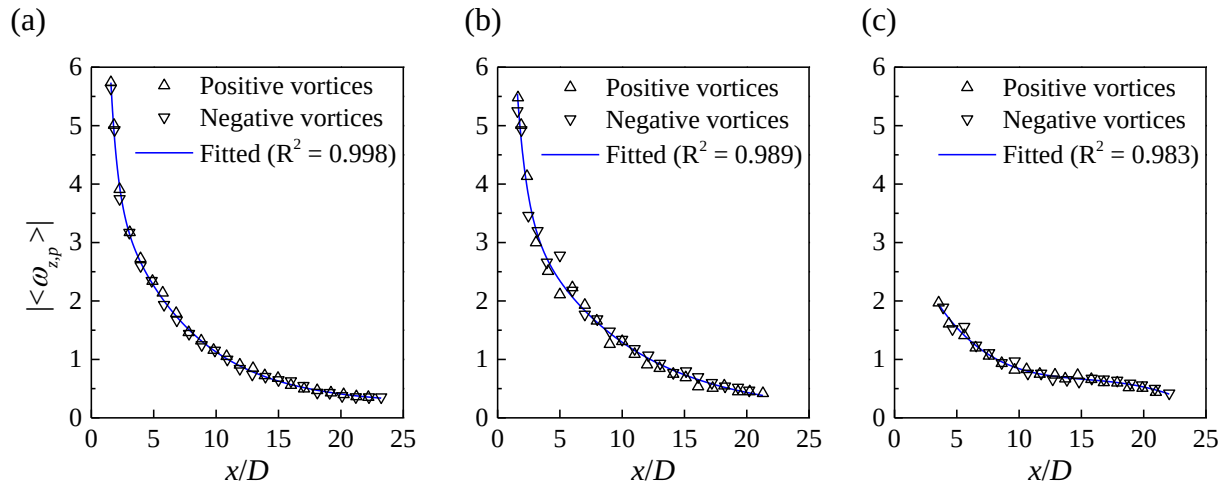

(d)

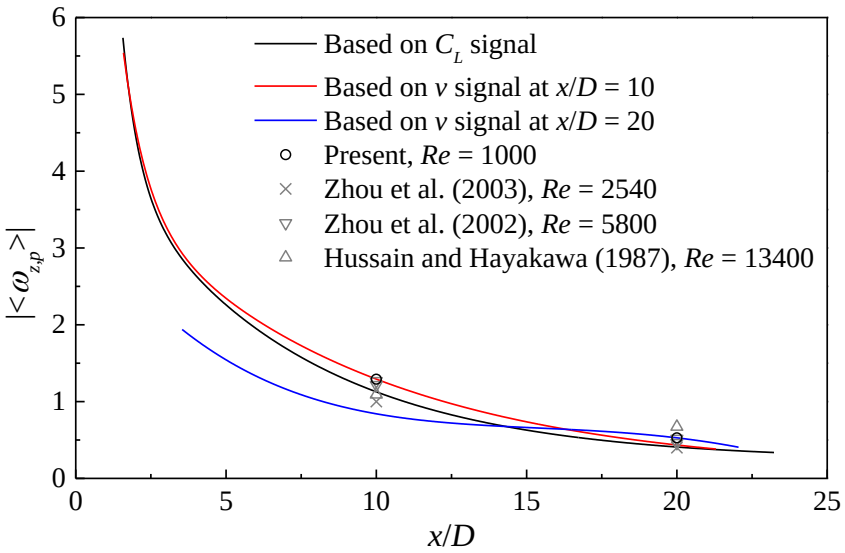

Fig. 5. Streamwise variation of the peak vorticity of the phase-averaged vortices in the turbulent wake of Re = 1000, determined based on the reference signal of (a) the lift coefficient (i.e. at x/D ~ 0), (b) transverse velocity v sampled at x/D = 10, and (c) transverse velocity v sampled at x/D = 20. Panel (d) shows a comparison of the present results with those reported by Hussain and Hayakawa (1987), Zhou et al. (2002) and Zhou et al. (2003).

Fig. 5(d) also shows a comparison of the present results for the turbulent wake of Re = 1000 (the open circles) with those reported by Hussain and Hayakawa (1987), Zhou et al. (2002) and Zhou et al. (2003) based on physical experiments at different Re values. The relatively good agreement between the present results and those reported in the literature (especially Zhou et al. (2002)) suggests that the primary vortex street may undergo a similar decay with distance downstream over a range of subcritical Re.

Similar to the determination of the peak vorticity of the phase-averaged vortices at x/D = 10 and 20 in Fig. 5, Table 1 summarises the transverse location of the peak vorticity (y_c/D) and the advection velocity of the vortex (U_c/U) at $y = y_c$ for x/D = 10 and 20. The present results agree relatively well with the experimental results by Zhou et al. (2003), Zhou et al. (2002) and Hussain and Hayakawa (1987).

Table 1. Characteristics of the phase-averaged vortices at x/D = 10 and 20.

	Re	x/D = 10		x/D = 20	
		y_c/D	U_c/U	y_c/D	U_c/U
Present	1000	0.25	0.84	0.67	0.87
Zhou et al. (2003)	2540	0.29	0.865	0.63	0.861
Zhou et al. (2002)	5800	0.23	0.86	0.80	0.87
Hussain and Hayakawa (1987)	13400		0.87		0.875

3.2. Spectral analysis of decay of the primary vortex street

In addition to the streamwise variation of the peak vorticity of the phase-averaged vortices shown in Fig. 5(d), the decay of the primary vortex street with distance downstream can also be quantified by the frequency spectra of v sampled at various streamwise locations along $y/D = 0$ (Fig. 6) and $y/D = 1.5$ (Fig. 7). The frequency spectra are determined from the FFT of the time histories of v, where A and f denote the amplitude and frequency of v, respectively. Each frequency spectrum shown in Fig. 6 and Fig. 7 is an average of the frequency spectra derived from the time histories of v sampled at 16 equally-spaced spanwise locations. Each time history of v is sampled over a time period of $100T$ with a sample interval of $6\Delta t^*$ (= 0.01875). The resultant frequency spectrum has a frequency resolution of $\Delta fD/U = 0.00207$.

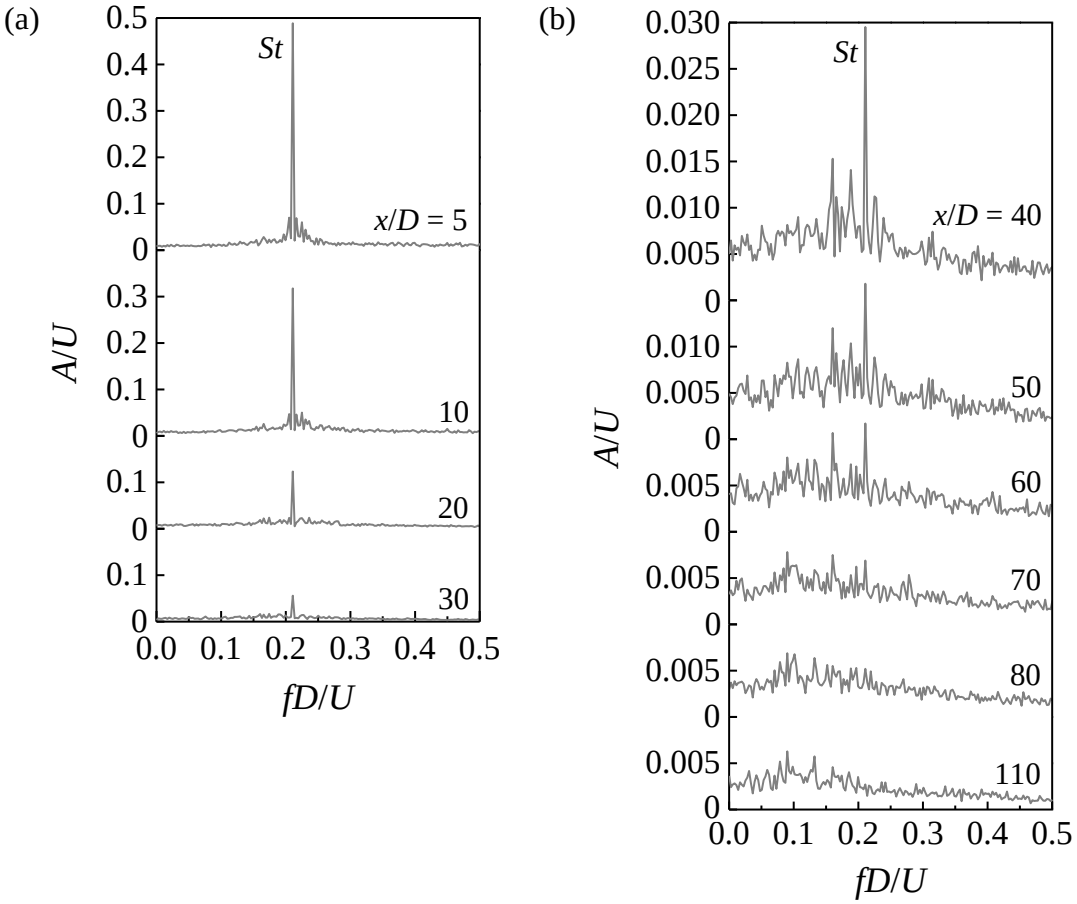

Fig. 6. Frequency spectra of v sampled at various streamwise locations along the wake centreline ($y/D = 0$) for the turbulent wake of $Re = 1000$: (a) $x/D = 5 – 30$, and (b) $x/D = 40 – 110$.

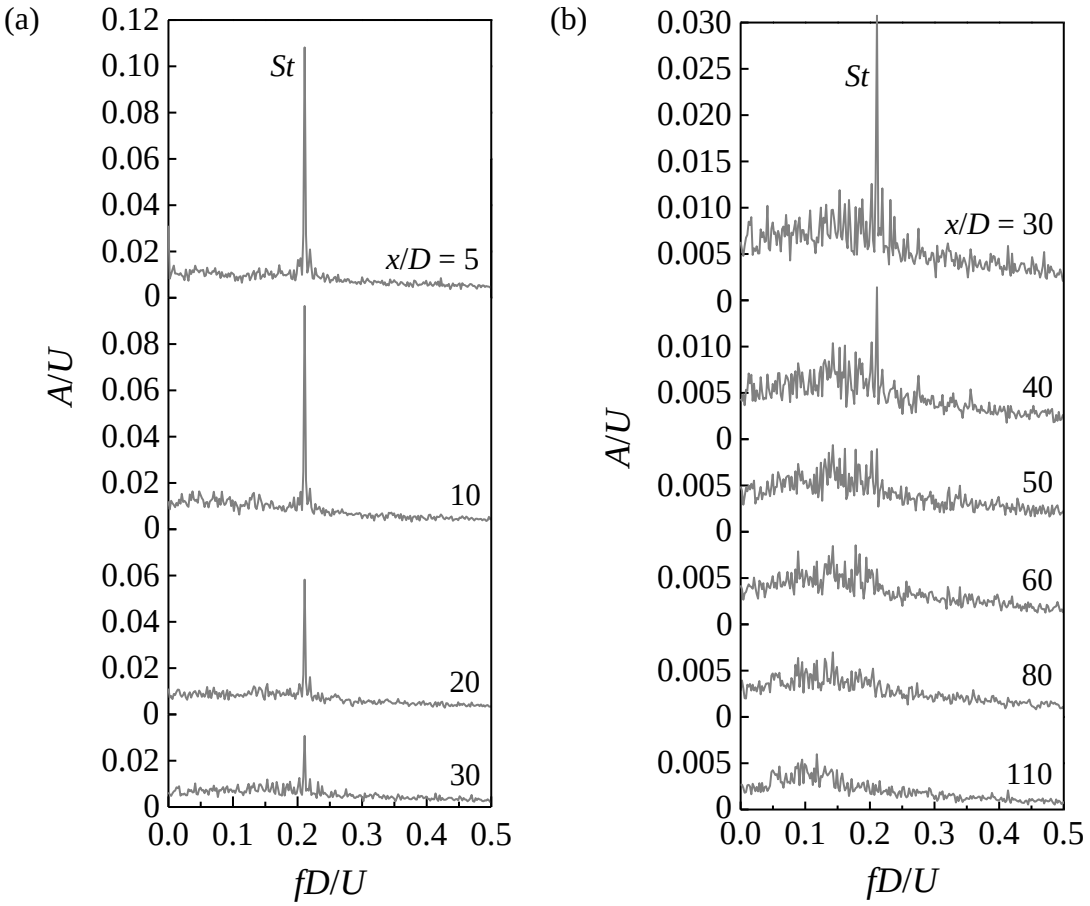

Fig. 7. Frequency spectra of v sampled at various streamwise locations along y/D = 1.5 for the turbulent wake of Re = 1000: (a) x/D = 5 – 30, and (b) x/D = 30 – 110.

As shown in Fig. 6(a) and Fig. 7(a), the relatively near wake of the cylinder is dominated by a well-defined frequency corresponding to the primary vortex shedding (i.e. St). The decrease in the amplitude of v at St with distance downstream is quantified in Fig. 8(a). In particular, an exponential decay of the amplitude at St is observed for y/D = 0 over x/D = 5–30. Based on a curve fitting of this range, the decay rate of the primary vortex street is 0.0380 decades/D, where decade stands for an order of magnitude in A. Fig. 9 summarises the decay rates for different Re values, including those determined in the present study and those by Cimbala et al. (1988) using the v signal. The decay rate increases approximately linearly over the range of Re investigated.

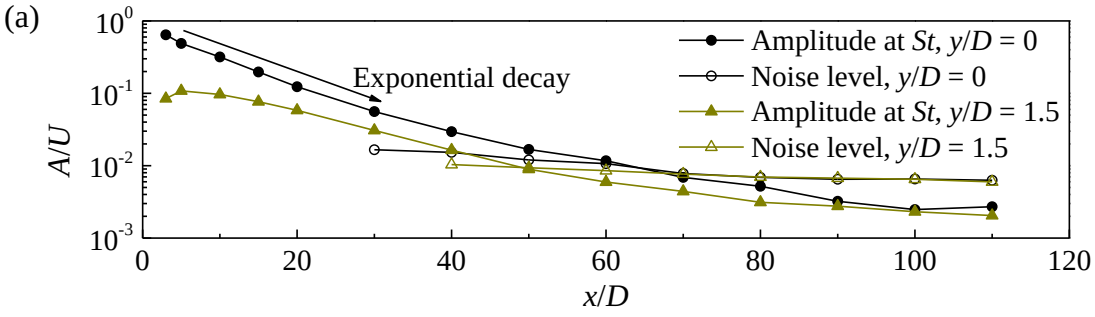

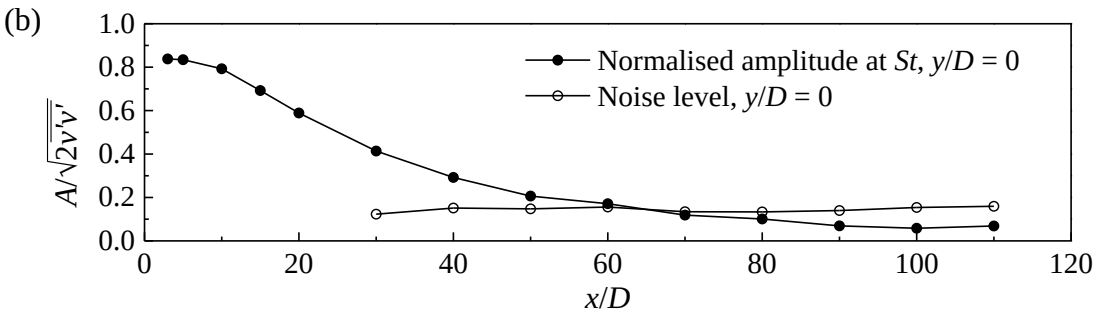

Fig. 8. Streamwise variations of (a) the amplitude of v at St, and (b) the normalised amplitude of v at St.

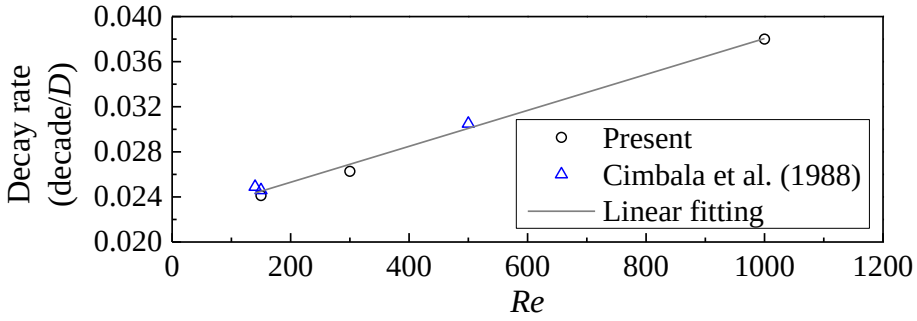

Fig. 9. Decay rate of the primary vortices predicted at different Re values. The decay rate is determined as the decrease in the spectral amplitude of v at St with distance downstream.

As shown in Fig. 6(b) and Fig. 7(b) and further quantified in Fig. 8(a), the amplitude at St decreases gradually with distance downstream and dives into the noise level (quantified by the largest amplitude other than that at St). Based on a linear interpolation, the frequency peak at St disappears at x/D = 64 for y/D = 0 but earlier at x/D = 49 for y/D = 1.5 (a convergence check of the x/D value with respect to several key numerical parameters is reported in Appendix C). The reason for the difference is that although the positive (or negative) primary vortices mainly travel along y/D ~ 1.5 (or y/D ~ –1.5) over the streamwise range of at least x/D ~ 50–60 (Fig. 4), the alternate passage of the positive and negative vortices near the wake centreline still induces a larger amplitude of v at St at y/D = 0 than that at y/D = 1.5 (Fig. 8a), such that the St peak can be detected more downstream at y/D = 0.

Similarly, Roshko (1954) found that for the turbulent wakes of Re = 500–4000, the discrete energy at St disappeared and the wake became completely turbulent at x/D = 40–50. Compared with the present results, the slightly smaller x/D identified by Roshko (1954) was likely affected by the transverse locations of y/D > 1.5 for the measurement of the frequency spectra at x/D = 24 and 48. On the other hand, Browne et al. (1989) found that for the turbulent wake of Re = 1170, the discrete energy at St disappeared at x/D ~ 75, which was partly because their measurement was taken at the transverse location of maximum signal strength.

As the wake becomes increasingly turbulent with distance downstream, the energy in the wake may transfer from St to other frequencies. In order to reveal the

energy transfer, the amplitude of v at St (Fig. 8a) is normalised by $\sqrt{2\overline{v'v'}}$ (Fig. 8b). Such a normalisation removes the influence of the fluctuating amplitude of the v signal and reveals the relative strengths of different frequency components. For example, when the time history of v is sinusoidal with a single frequency St and arbitrary amplitude, the normalised amplitude becomes 1.0. For the laminar primary vortex street, the normalised amplitude is very close to 1.0 (Jiang and Cheng, 2019). For the turbulent wake at Re = 1000, however, the normalised amplitude of v at St decreases monotonically with distance downstream (Fig. 8b), which suggests that the velocity fluctuation is decreasingly contributed by the primary vortices and increasingly contributed by the turbulence.

3.3. Three components of the kinetic energy dissipation rate

As introduced in section 1, the total kinetic energy dissipation rate ε consists of the contributions from the mean flow, the coherent primary vortices and the remainder, which are denoted ε_m, $\tilde{\varepsilon}$ and ε_r and determined by equations (1.6)–(1.8), respectively. Owing to the random distribution of the rib-like streamwise vortices (Fig. 1c) and the associated turbulence along the spanwise direction, at any specific point in the flow field the mean spanwise velocity and the phase-averaged spanwise velocity should be zero, such that equations (1.6) and (1.7) can be reduced to:

$$\varepsilon_m = \nu \frac{\partial u_{m,i}}{\partial x_j}\left(\frac{\partial u_{m,i}}{\partial x_j} + \frac{\partial u_{m,j}}{\partial x_i} \right) \qquad (i, j = 1, 2), \tag{3.1}$$

$$\tilde{\varepsilon} = \nu \overline{\frac{\partial \tilde{u}_i}{\partial x_j}\left(\frac{\partial \tilde{u}_i}{\partial x_j} + \frac{\partial \tilde{u}_j}{\partial x_i} \right)} \qquad (i, j = 1, 2). \tag{3.2}$$

Practically, the ε_m and $\tilde{\varepsilon}$ values determined by equations (1.6) and (1.7) may be slightly larger than those determined by equations (3.1) and (3.2). This is because the time-averaged and phase-averaged flows are obtained from finite statistical time periods, where small degrees of spanwise velocity (of the order of $0.01U$) may exist and contribute undesirably to ε_m and $\tilde{\varepsilon}$. To eliminate this effect, the present study uses equations (3.1) and (3.2) to calculate ε_m and $\tilde{\varepsilon}$. To further improve the statistical convergence, equation (3.1) is calculated based on the time- and span-averaged velocity field, while equation (3.2) is calculated based on the procedures introduced in section 2.3 (calculated at four equally-spaced spanwise locations). To maintain conservation of the total dissipation rate, ε_r is calculated as:

$$\varepsilon_r = \varepsilon - \varepsilon_m - \tilde{\varepsilon}, \tag{3.3}$$

where ε is calculated by equation (1.5) using the instantaneous 3D velocity fields.

Fig. 10 shows the span-averaged fields of ε_m, $\tilde{\varepsilon}$ and ε_r for the turbulent wake of Re = 1000, where the phase average is based on the C_L signal. It is also checked that by using the v signal sampled at x/D = 10, the $\tilde{\varepsilon}$ and ε_r fields are qualitatively similar. As shown in Fig. 10(a), the ε_m component is concentrated in the boundary layer and

the separating shear layer, which is in accordance with the mean shear of the flow around the cylinder. In contrast, the $\tilde{\varepsilon}$ and ε_r components shown in Fig. 10(b,c) develop in the wake region. The $\tilde{\varepsilon}$ field displays two peak regions away from the wake centreline, while the ε_r field peaks at the wake centreline (for $x/D \gtrsim 5$). The different peak regions for the $\tilde{\varepsilon}$ and ε_r components can be explained based on Fig. 22(c,d) in section 3.8, where the spatial distributions of the phase-averaged fields are presented.

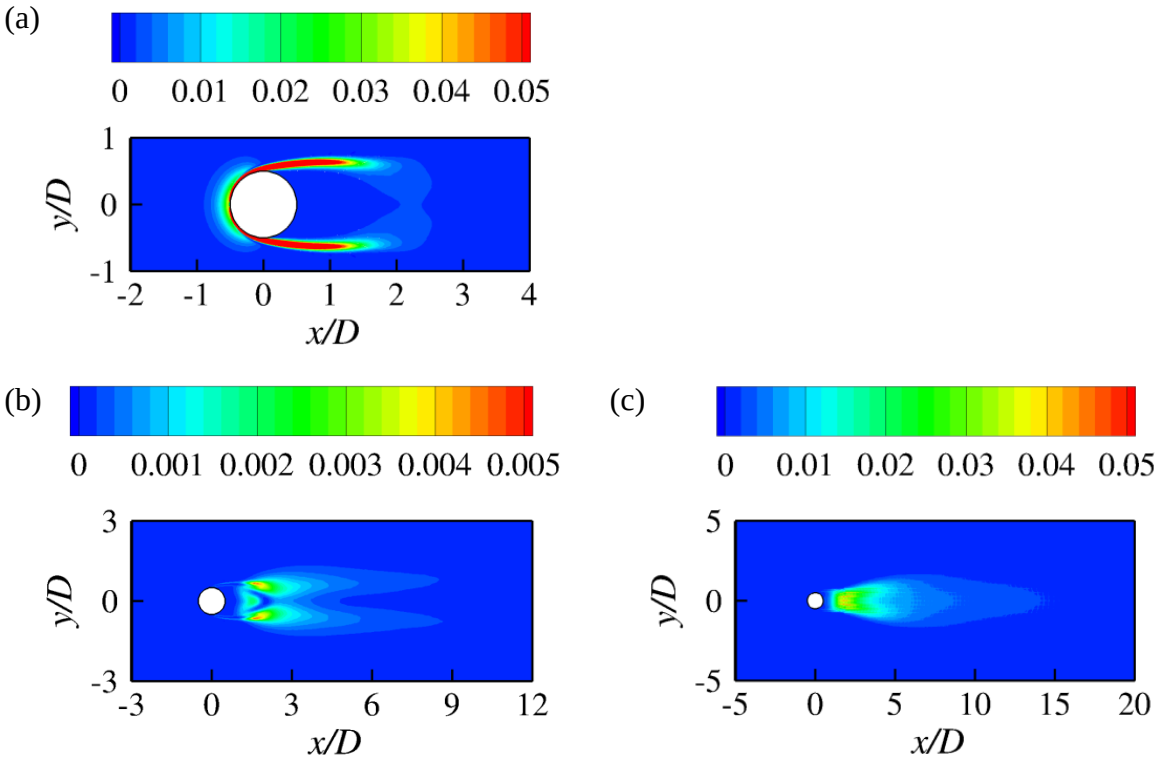

Fig. 10. Span-averaged fields of (a) $\varepsilon_m D/U^3$, (b) $\tilde{\varepsilon} D/U^3$, and (c) $\varepsilon_r D/U^3$.

The $\tilde{\varepsilon}$ and ε_r fields shown in Fig. 10(b,c) are qualitative patterns. Quantitatively, the transverse distribution of $\tilde{\varepsilon}$ at a specific x/D should be determined by extracting the coherent structures based on the v signals sampled at the corresponding x/D. For example, Fig. 11(a) illustrates the transverse distributions of $\tilde{\varepsilon}$ at x/D = 10 determined based on different reference signals. The largest $\tilde{\varepsilon}$ values at x/D = 10 are determined based on the v signals sampled at x/D = 10. Fig. 11(a) also illustrates the transverse distributions of ε_m, ε_r and ε at x/D = 10, which indicates that at a specific x/D, the three components of the dissipation rate (ε_m, $\tilde{\varepsilon}$ and ε_r) may peak at different transverse locations (also shown qualitatively in Fig. 10). Therefore, it is less meaningful to compare their values at a same transverse location (as was done in several previous studies). Instead, the contribution of each component at a specific x/D is quantified through integrating the corresponding component along the y-direction, such that its percentage contribution to the total ε can be determined.

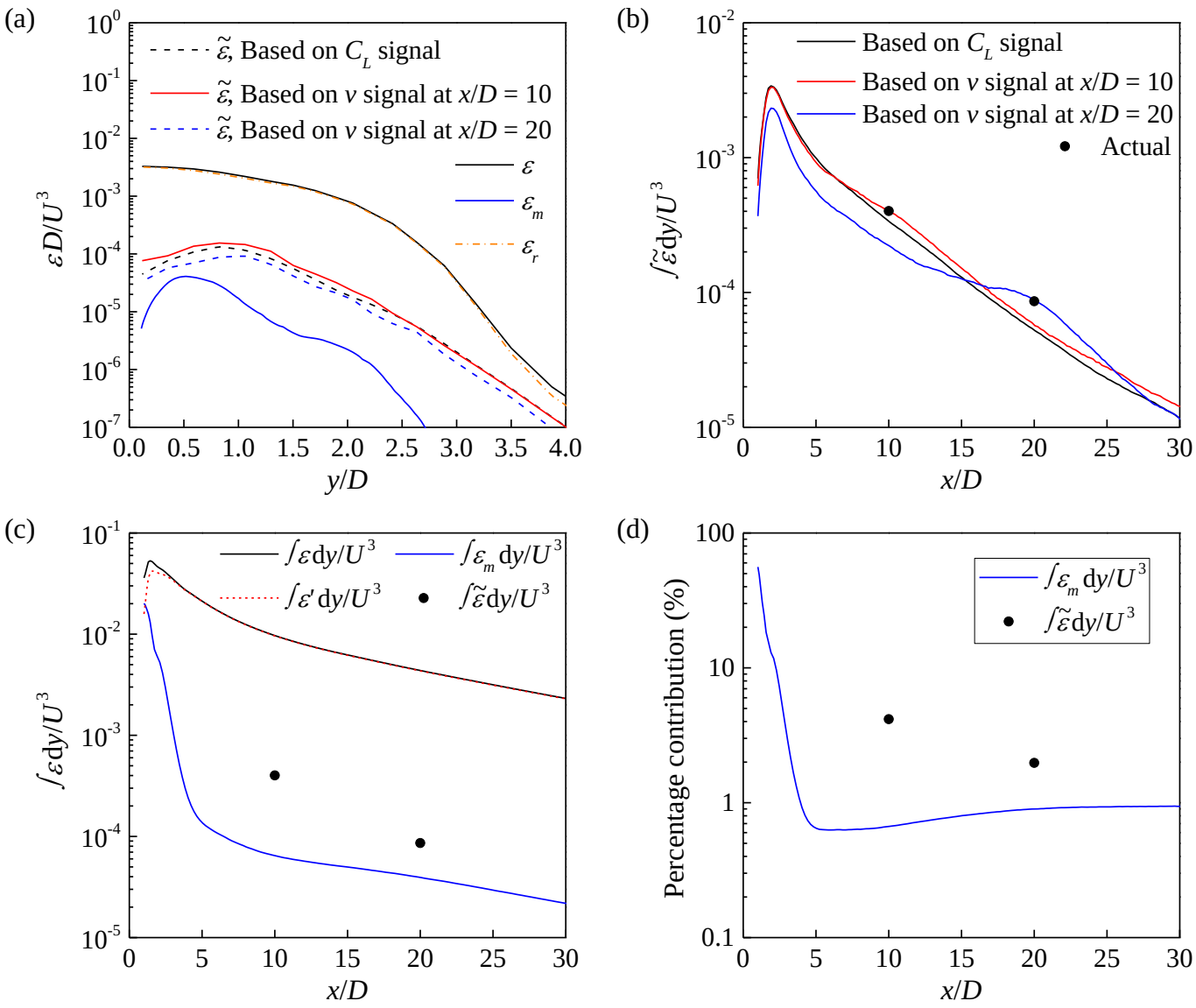

Fig. 11. (a) Transverse distribution of different components of the dissipation rate at x/D = 10. (b–d) Streamwise variation of the integrated dissipation rate: (b) the coherent component $\tilde{\varepsilon}$ determined based on different reference signals, (c) different components of the dissipation rate, and (d) percentage contribution of different components of the dissipation rate.

Fig. 11(b) shows the streamwise variations of the integrated $\tilde{\varepsilon}$ determined based on different reference signals. The effect of different reference signals is similar to that observed for the streamwise variation of the peak vorticity in Fig. 5(d), where the v signals sampled at x/D = 10 and 20 yield the largest results at x/D = 10 and 20, respectively (denoted by solid dots). Based on the C_L signal, the integrated $\tilde{\varepsilon}$ at x/D = 10 and 20 are under-predicted by 17% and 39%, respectively, which justifies the necessity of calculating $\tilde{\varepsilon}$ based on the coherent structures extracted at the corresponding x/D.

Fig. 11(c) shows the actual integrated $\tilde{\varepsilon}$ at x/D = 10 and 20, together with the integrated ε, ε_m and ε' (= $\varepsilon - \varepsilon_m$) values at various x/D. The integrated ε, ε_m and ε'

values are not limited at x/D = 10 and 20, because they are not related to how the coherent structures are extracted. The ε_m component, which is associated with the mean shear around the cylinder, decreases drastically and monotonically with distance downstream. The total fluctuation component ε' peaks at x/D ~ 1.5, which is consistent with the emergence of the primary and secondary vortices and the associated turbulence in the near wake, and then gradually decreases downstream.

Based on the results shown in Fig. 11(c), the percentage contributions of ε_m and $\tilde{\varepsilon}$ to the total ε are shown in Fig. 11(d). The percentage contribution of the ε_m component quickly drops to ~ 1% at x/D ~ 4 and remains at ~ 1% further downstream. The $\tilde{\varepsilon}$ component, which is associated with the coherent primary vortices, accounts for only 4.2% and 2.0% of the total ε at x/D = 10 and 20, respectively. In contrast, the remainder, which is induced by the rib-like streamwise vortices and the associated random turbulence that develop only in the 3D turbulent wake, accounts for the majority of the total ε for almost the entire wake (beyond the immediate neighbourhood of the cylinder), e.g. 95% and 97% for x/D = 10 and 20, respectively.

3.4. Twelve velocity derivative terms constituting the dissipation rate

In this section, the twelve velocity derivative terms constituting the dissipation rate are examined separately. To facilitate comparison of the present results with the experimental results of Chen et al. (2018), the total fluctuation component of the dissipation rate ε' is presented for both cases. The twelve velocity derivative terms for ε' are given on the right-hand side of the equation below.

$$\begin{aligned}\frac{\varepsilon'}{\nu} = {} & 2\overline{\left(\frac{\partial u'}{\partial x}\right)^2} + \overline{\left(\frac{\partial v'}{\partial x}\right)^2} + \overline{\left(\frac{\partial w'}{\partial x}\right)^2} + \overline{\left(\frac{\partial u'}{\partial y}\right)^2} + 2\overline{\left(\frac{\partial v'}{\partial y}\right)^2} + \overline{\left(\frac{\partial w'}{\partial y}\right)^2} \\ & + \overline{\left(\frac{\partial u'}{\partial z}\right)^2} + \overline{\left(\frac{\partial v'}{\partial z}\right)^2} + 2\overline{\left(\frac{\partial w'}{\partial z}\right)^2} + 2\overline{\frac{\partial u'}{\partial y}\frac{\partial v'}{\partial x}} + 2\overline{\frac{\partial u'}{\partial z}\frac{\partial w'}{\partial x}} + 2\overline{\frac{\partial v'}{\partial z}\frac{\partial w'}{\partial y}}\end{aligned} \tag{3.4}$$

Fig. 12 illustrates the transverse distribution of the term $2\overline{\left(\partial u'/\partial x\right)^2}$ at x/D = 10, 20 and 40 in the turbulent wake of Re = 1000. After normalising the term into $2\overline{\left(\partial u'/\partial x\right)^2}/\left(U/D\right)^2$, a comparison is made between the present results and the experimental results by Chen et al. (2018) at Re = 2500. The reason why the term $2\overline{\left(\partial u'/\partial x\right)^2}$ is chosen for the comparison with the experimental results is that (i) among the twelve velocity derivative terms listed in equation (3.4), this term can be most easily and confidently measured by physical experiments (Browne et al., 1987; Chen et al., 2018), and (ii) this is an important term, which will be used later on as a reference for evaluating local isotropy of the flow. Based on equations (B.6), (B.7) and (3.4), the results by Chen et al. (2018) at Re = 2500 are multiplied by 1000/2500 = 0.4 for a direct comparison with the present results at Re = 1000. Chen et al. (2018) also mentioned that in their experiments "the velocity derivatives are considered to be

underestimated by approximately 18%–7% at x/D = 10–40", due to limited spatial resolution of the probes. Therefore, the normalised velocity derivative terms (i.e. square of velocity derivative) by Chen et al. (2018) at x/D = 10, 20 and 40 are further divided by $(1 - 0.18)^2$, $(1 - 0.10)^2$, $(1 - 0.07)^2$, respectively, and the adjusted results are also shown in Fig. 12. The adjusted results agree relatively well with the present results, especially near the wake centreline where the magnitude of $2\overline{(\partial u'/\partial x)^2}$ is the largest.

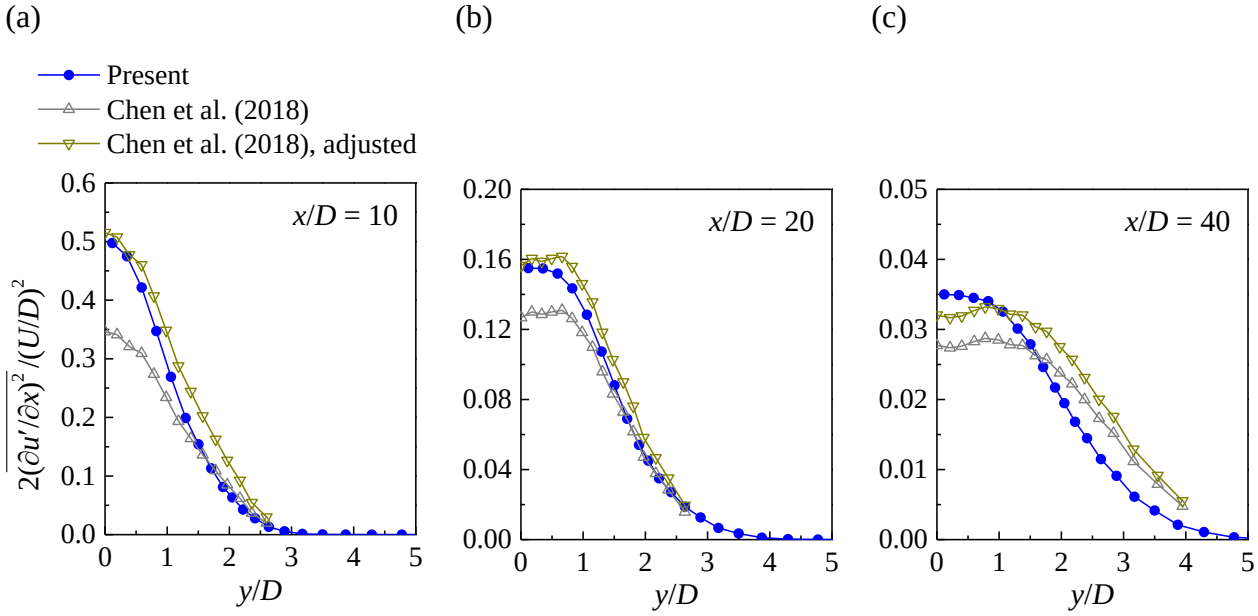

Fig. 12. Transverse distribution of the term $2\overline{(\partial u'/\partial x)^2}$ at (a) x/D = 10, (b) x/D = 20, and (c) x/D = 40.

After demonstrating a relatively close agreement between the present study and Chen et al. (2018) in predicting the term $2\overline{(\partial u'/\partial x)^2}$, Fig. 13 shows all twelve velocity derivative terms predicted by the present study (left column) and the ten terms predicted by Chen et al. (2018) (right column). To facilitate comparison between the two studies, the velocity derivative terms are normalised by the streamwise velocity deficit at the wake centreline (U_0) and the wake half-width (L) determined at the corresponding streamwise location. Specifically, U_0 is the difference between the free-stream velocity U and the mean streamwise velocity at the wake centreline, while L is the transverse distance between the wake centreline and the location where the streamwise velocity deficit is $U_0/2$.

As shown in Fig. 13, a major difference between the present results (left column) and those by Chen et al. (2018) (right column) is that, for the measurements made at each x/D (each row), the present results show a more isotropic dissipation, i.e. the first nine terms on the right-hand side of equation (3.4) (i.e. the square terms) converge towards $2\overline{(\partial u'/\partial x)^2}$, while the last three terms (i.e. the correlation terms) converge

towards $-\overline{(\partial u'/\partial x)^2}$ (shown by the plain dashed line in Fig. 13). In contrast, the results predicted by Chen et al. (2018) are far from isotropy even at x/D = 40. Although the square terms predicted by Chen et al. (2018) show a gradual convergence towards $2\overline{(\partial u'/\partial x)^2}$ with distance downstream (Fig. 13b,d,f), the correlation terms remain close to zero over x/D = 10–40, rather than converging towards $-\overline{(\partial u'/\partial x)^2}$ with distance downstream. This is inconsistent with the theoretical expectation that the flow becomes increasingly isotropic with distance downstream (if secondary flow features, e.g. oblique shedding and secondary vortex street (Williamson and Prasad, 1993), do not set in and alter the far wake). A possible explanation is that in physical experiments it is extremely difficult to measure the correlation terms accurately. "Because of the volume occupied by the two probes, phase differences between such quantities as $\partial u'/\partial y$ and $\partial v'/\partial x$ are likely to degrade the correlation $\overline{(\partial u'/\partial y)(\partial v'/\partial x)}$" (Browne et al., 1987). Naturally, this phase problem does not affect determination of the square terms (Browne et al., 1987). Nevertheless, moderate differences between the present results and those by Chen et al. (2018) are still observed in Fig. 13, which may be contributed by (i) differences in the Reynolds numbers, including possible influence from the shear-layer instability at Re = 2500 (but not at Re = 1000), (ii) the use of Taylor's hypothesis for several terms whereas direct measurement for other terms in the experiments, (iii) different levels of difficulties for the measurement of different velocity derivative terms using the hot-wire probes (Browne et al., 1987), etc.

As shown in section 3.3, the coherent component $\tilde{\varepsilon}$ still plays a role in the relatively near wake of x/D = 10. Fig. 14 decomposes the velocity derivative terms shown in Fig. 13(a) (for x/D = 10 and Re = 1000) into the coherent and remainder contributions. As shown in Fig. 14(a), the coherent contribution is mainly induced by the terms $\overline{(\partial \tilde{v}/\partial x)^2}$ and $2\overline{(\partial \tilde{u}/\partial y)(\partial \tilde{v}/\partial x)}$ at $y/L \lesssim 1$ (where the coherent structures are strong; see Fig. 4). The coherent contribution explains why in Fig. 13(a) the terms $\overline{(\partial v'/\partial x)^2}$ and $2\overline{(\partial u'/\partial y)(\partial v'/\partial x)}$ are the largest among the square and correlation terms, respectively, for the region near the wake centreline. After removing the coherent contribution, Fig. 14(b) shows that the terms $\overline{(\partial v_r/\partial x)^2}$ and $2\overline{(\partial u_r/\partial y)(\partial v_r/\partial x)}$ are no longer particularly large.

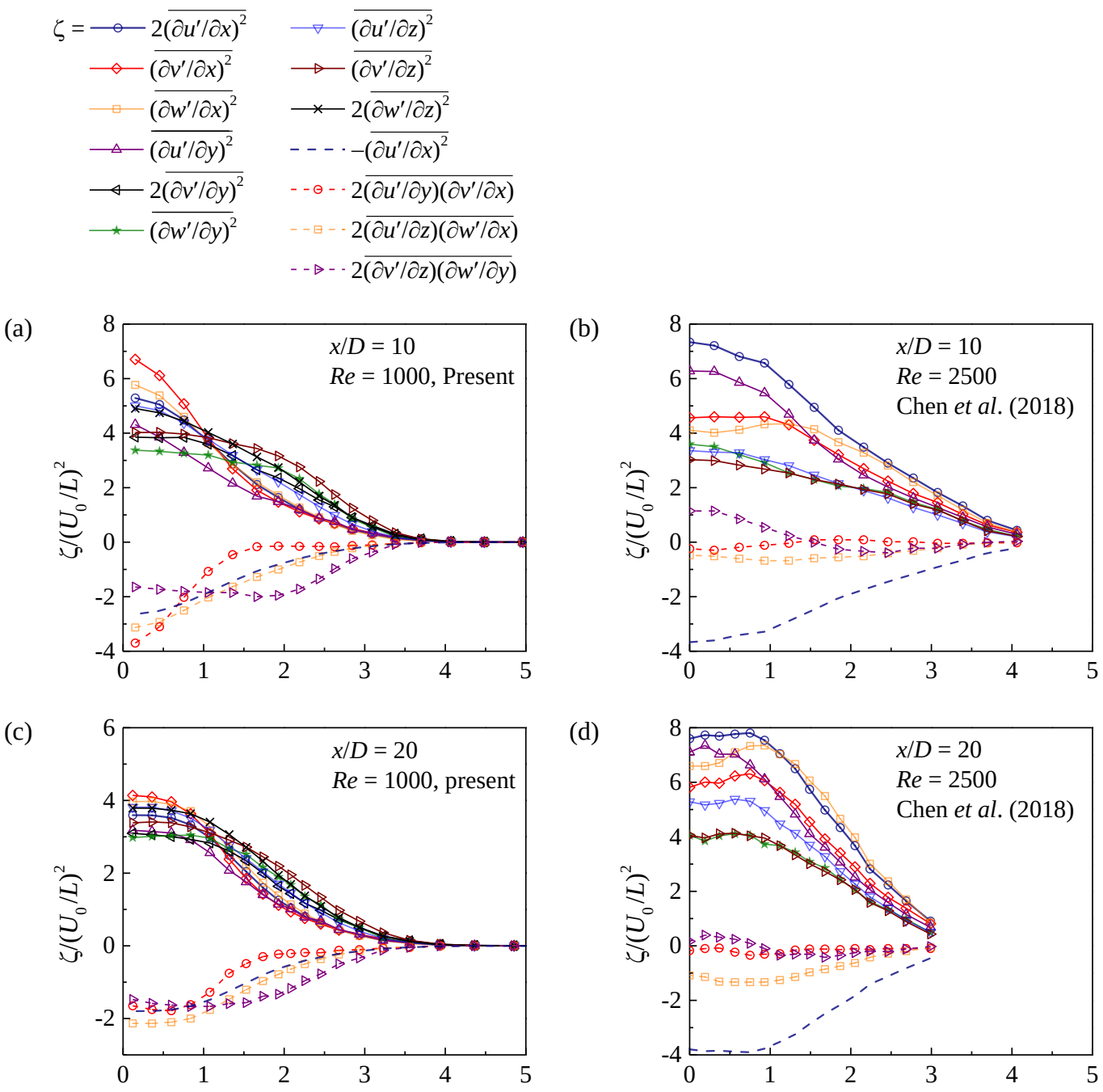
ζ =
2(∂u′/∂x)²
(∂u′/∂z)²
(∂v′/∂x)²
(∂v′/∂z)²
(∂w′/∂x)²
2(∂w′/∂z)²
(∂u′/∂y)²
−(∂u′/∂x)²
2(∂v′/∂y)²
2(∂u′/∂y)(∂v′/∂x)
(∂w′/∂y)²
2(∂u′/∂z)(∂w′/∂x)
2(∂v′/∂z)(∂w′/∂y)
(a)
x/D = 10
Re = 1000, Present
ζ/(U0/L)²
(b)
x/D = 10
Re = 2500
Chen et al. (2018)
ζ/(U0/L)²
(c)
x/D = 20
Re = 1000, present
ζ/(U0/L)²
(d)
x/D = 20
Re = 2500
Chen et al. (2018)
ζ/(U0/L)²

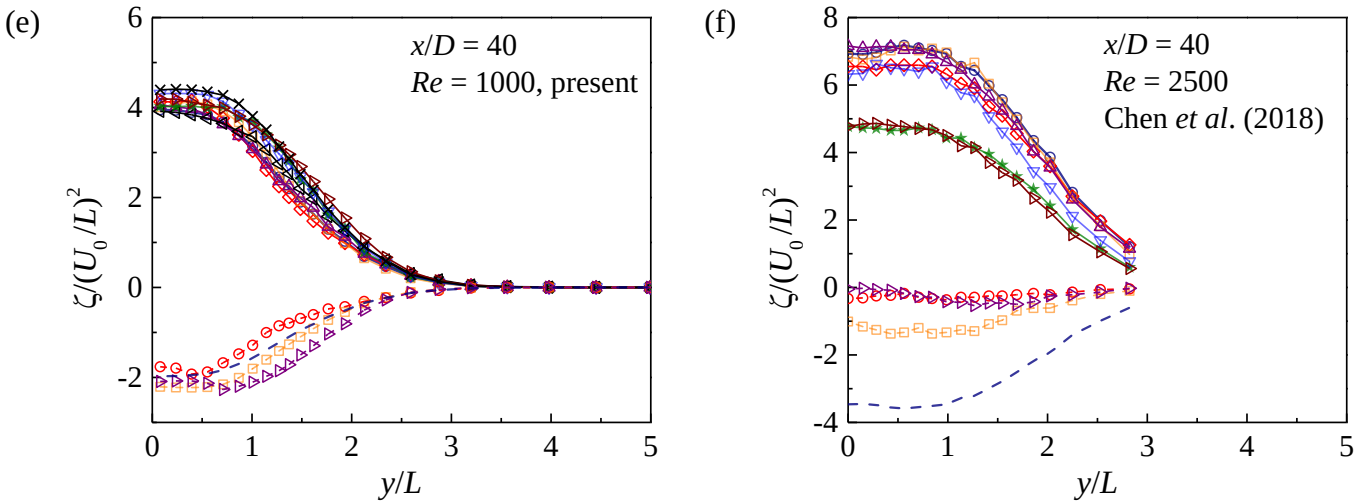

Fig. 13. Transverse distributions of the twelve velocity derivative terms (denoted ζ) constituting the total dissipation rate. (a) x/D = 10, Re = 1000 (present), (b) x/D = 10, Re = 2500 (Chen et al., 2018), (c) x/D = 20, Re = 1000 (present), (d) x/D = 20, Re = 2500 (Chen et al., 2018), (e) x/D = 40, Re = 1000 (present), and (f) x/D = 40, Re = 2500 (Chen et al., 2018).

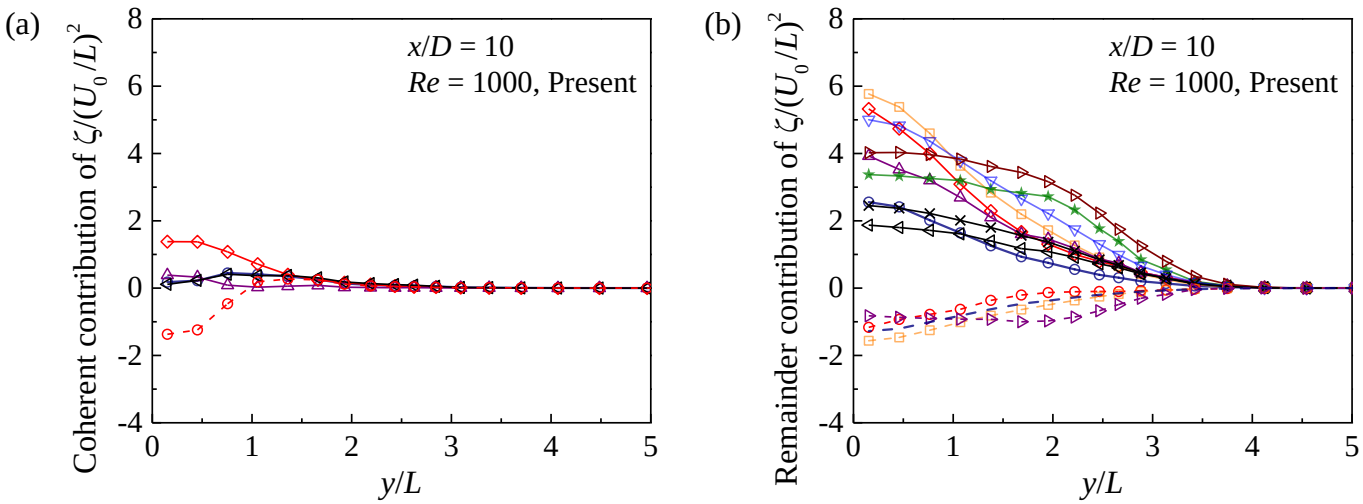

Fig. 14. Decomposition of the velocity derivative terms for x/D = 10 and Re = 1000 (Fig. 13a) into (a) the coherent contribution, and (b) the remainder contribution. The legend for the velocity derivative terms follows that used in Fig. 13.

3.5. Surrogates of the dissipation rate

With the availability of the true dissipation rate ε' (calculated based upon all twelve velocity derivative terms) in the present study, the performances of the four surrogates given in equations (1.10)–(1.13) can be evaluated. To be consistent with the previous experimental studies (e.g. Browne et al., 1987; George and Hussein, 1991; Chen et al., 2018) which reported surrogates of the dissipation rate based on the ε' component, the present study also considers the ε' component (rather than ε or ε_r).

Because the contribution of $\tilde{\varepsilon}$ to ε is less than 2% at $x/D > 20$, presumably it becomes unnecessary to decompose ε' into $\tilde{\varepsilon}$ and ε_r.

Fig. 15(a) shows the true dissipation rate ε' and its surrogates sampled along the wake centreline, while Fig. 16 shows those sampled transversely at various streamwise locations. As a common practice to reflect the self-preservation nature of the relatively far wake (e.g. Tang et al., 2016; Chen et al., 2018), the dissipation rate is normalised by U_0 and L. In addition, Fig. 15(b) shows the relative differences of the surrogates to ε' along the wake centreline. Based on Fig. 15 and Fig. 16, the performances of the surrogates are summarised below, where a good agreement with ε' is defined as a relative difference of less than 2%.

(i) The surrogate ε'_{yz} agrees well with ε' over almost the entire wake ($x/D \gtrsim 5$).
(ii) The surrogate ε'_{hom} agrees well with ε' for $x/D \gtrsim 20$.
(iii) The surrogate ε'_{axis} agrees well with ε' for $x/D \gtrsim 40$. For $x/D \sim 20$–35, ε'_{axis} displays a slight overestimation of ε' (~ 4%–2%) near the wake centreline.
(iv) The surrogate ε'_{iso} does not match ε' for the entire wake.

On a side note, Lefeuvre et al. (2014) evaluated the performances of these surrogates for a square cylinder wake, and found that all four surrogates performed well at x/D = 20, 60 and 100, except for a mismatch between ε'_{iso} and ε' at x/D = 20. The better performances of the surrogates for the square cylinder wake (e.g. an agreement between ε'_{iso} and ε' at x/D = 60 and 100) suggest that the square cylinder wake is more isotropic than the circular cylinder wake (Lefeuvre et al., 2014).

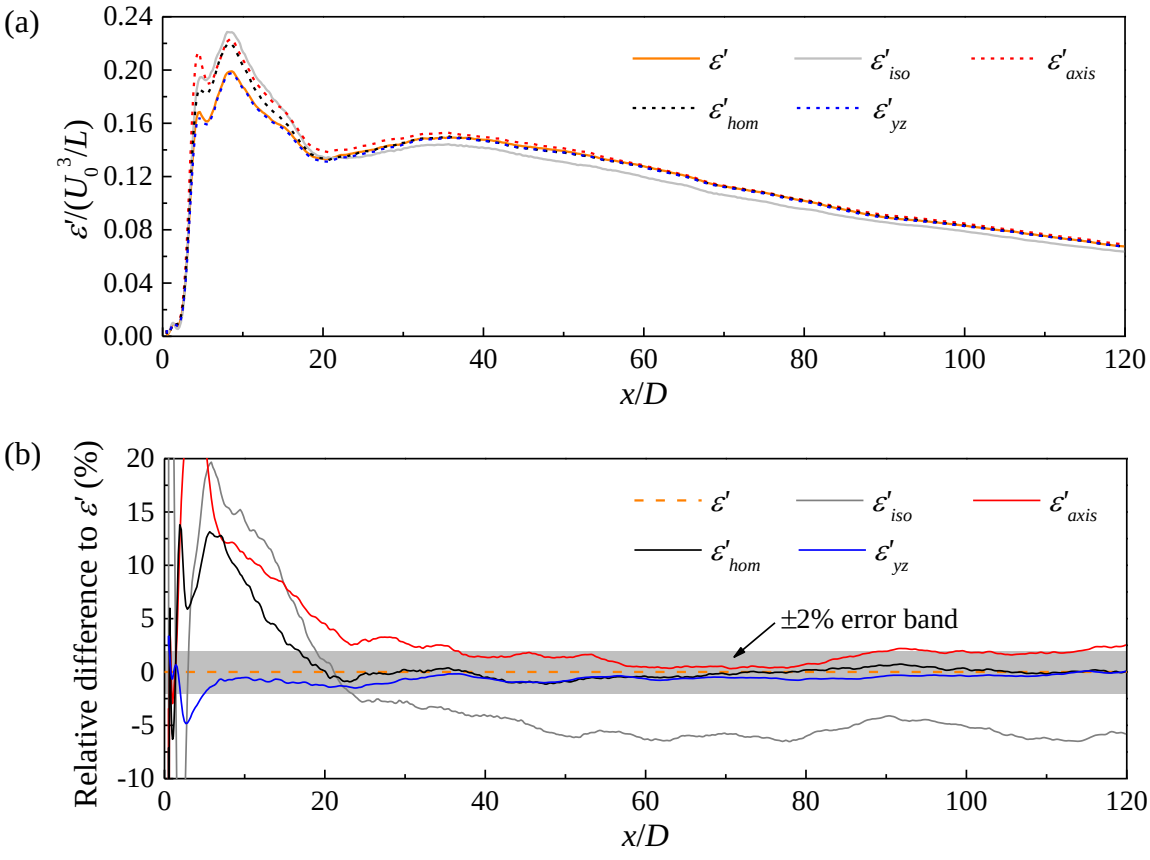

Fig. 15. (a) Streamwise variations of the true dissipation rate ε' and its surrogates

along the wake centreline, and (b) relative differences of the surrogates to ε'. The shaded area represents an error band of $\pm 2\%$.

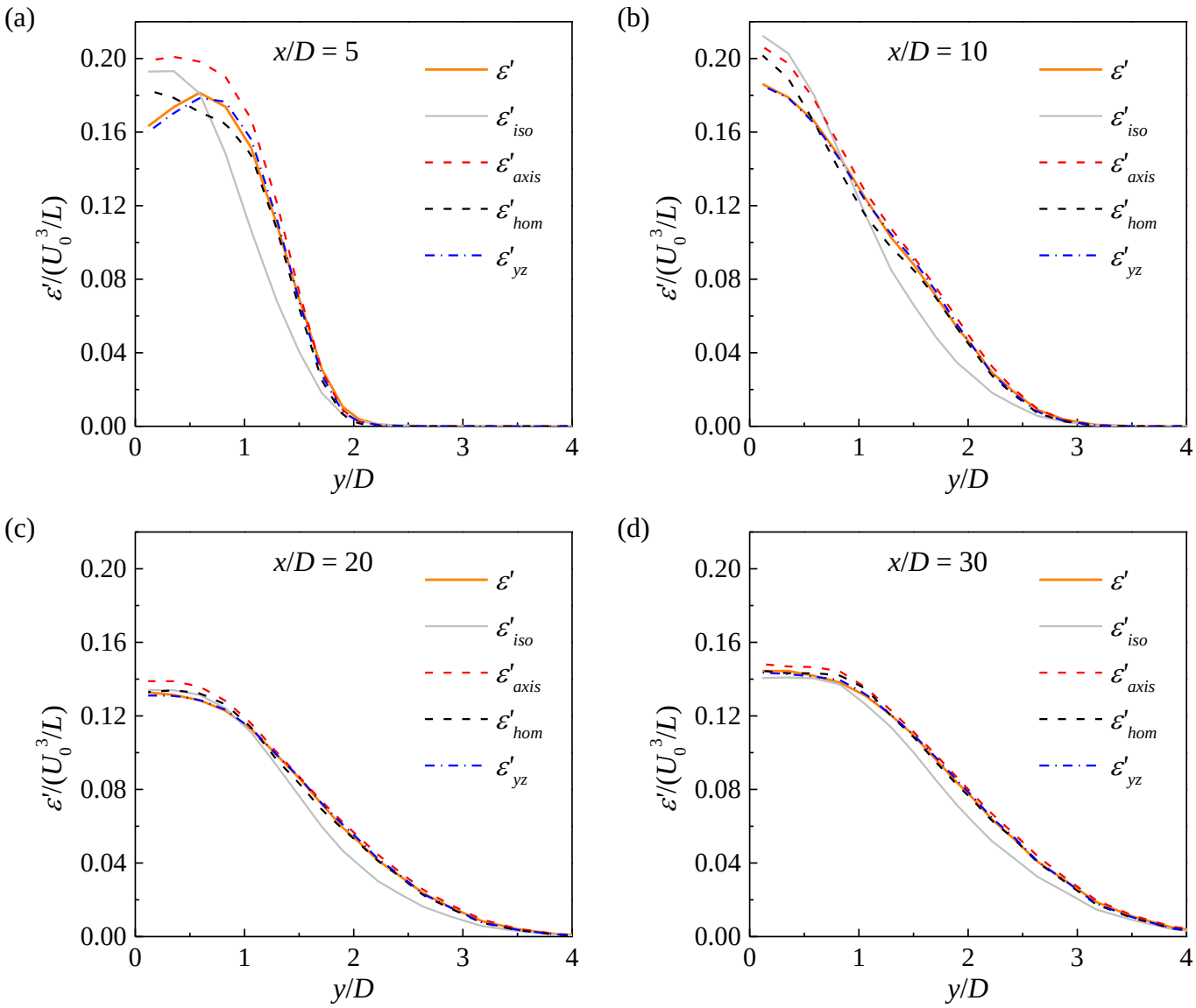

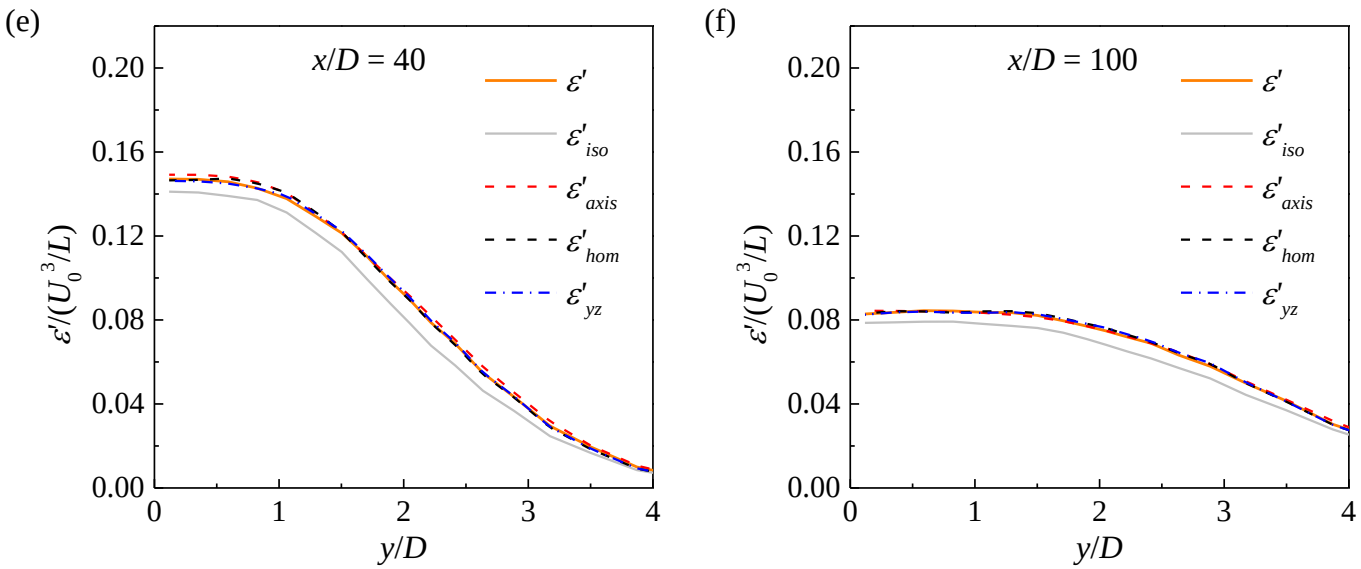

Fig. 16. Transverse distributions of the true dissipation rate ε' and its surrogates at specific streamwise locations: (a) x/D = 5, (b) x/D = 10, (c) x/D = 20, (d) x/D = 30, (e) x/D = 40, and (f) x/D = 100.

Since the coherent contribution $\tilde{\varepsilon}$ still accounts for 4.2% and 2.0% of ε at x/D = 10 and 20, respectively (Fig. 11d), its effect on the performance of the surrogates is examined. Because the coherent component is by no means isotropic, axisymmetric or homogeneous, removing the coherent component may result in improved performances of the surrogates. Fig. 17 shows the transverse distributions of ε_r and its surrogates at x/D = 10 and 20. A comparison between Fig. 17 and Fig. 16(b,c) suggests that, after removing the coherent component, the surrogates to ε_r indeed show better performances than the surrogates to ε'.

(i) The surrogate $\varepsilon_{r,hom}$ agrees well with ε_r as early as x/D = 10. Specifically, the relative difference to the true value at the wake centreline reduces from 8.4% to 1.3%.

(ii) The surrogate $\varepsilon_{r,axis}$ agrees well with ε_r as early as x/D = 20. Specifically, the relative difference to the true value at the wake centreline reduces from 4.7% to 1.6%. At x/D = 10, the degree of overestimation is also reduced (the relative difference to the true value at the wake centreline reduces from 10.9% to 4.6%).

(iii) Nevertheless, the surrogate $\varepsilon_{r,iso}$ still mismatches ε_r.

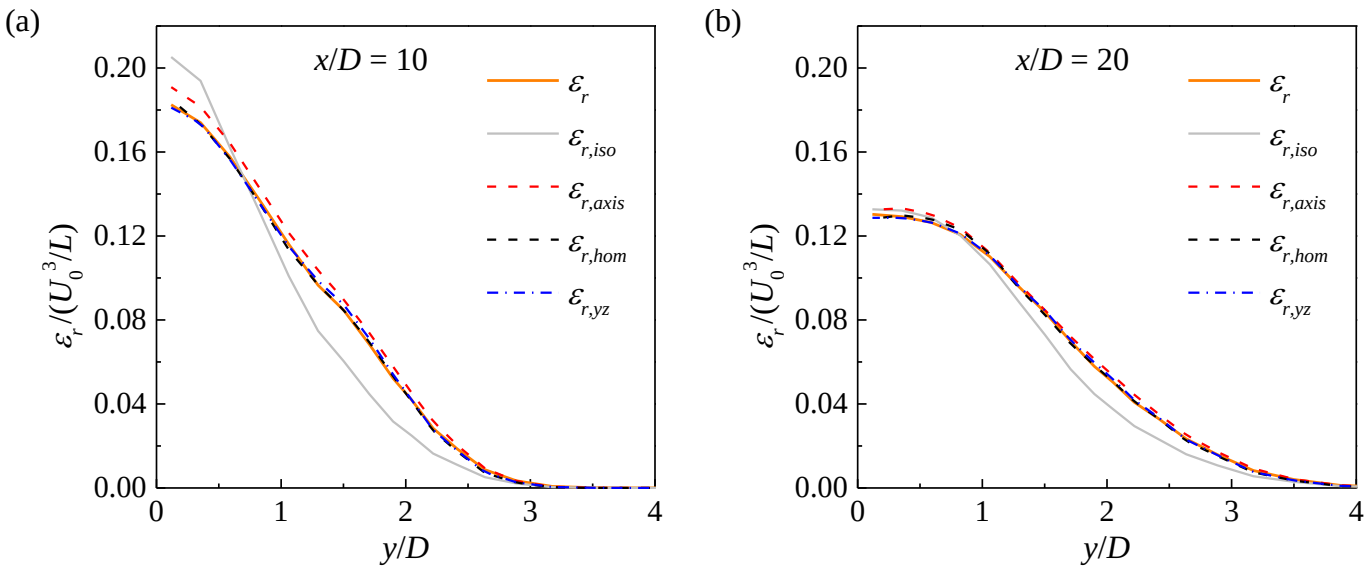

Fig. 17. Transverse distributions of the true dissipation rate ε_r and its surrogates at specific streamwise locations: (a) x/D = 10, and (b) x/D = 20.

3.6. Validity of local isotropy, axisymmetry and homogeneity

The agreement between the true dissipation rate and a surrogate may not necessarily indicate that the turbulent dissipation is truly locally axisymmetric or locally homogeneous. Rather, errors induced by the approximations to the unmeasured velocity derivative terms may offset one another, resulting in a good performance of the surrogate as a whole (Antonia et al., 1998). To examine the validity of local isotropy, local axisymmetry, local homogeneity and homogeneity in the *y*-*z* plane, the approximations for the unmeasured velocity derivative terms are examined individually, where the ratios A_i, B_i, C_i and D_i between the approximated value and the corresponding unmeasured velocity derivative term are determined. Specifically, local isotropy (Taylor, 1935) contains eleven approximations with A_i = 1:

$$A_1=\overline{\left(\frac{\partial u_r}{\partial x}\right)^2}\Big/\overline{\left(\frac{\partial v_r}{\partial y}\right)^2},\quad A_2=\overline{\left(\frac{\partial u_r}{\partial x}\right)^2}\Big/\overline{\left(\frac{\partial w_r}{\partial z}\right)^2},\quad A_3=2\overline{\left(\frac{\partial u_r}{\partial x}\right)^2}\Big/\overline{\left(\frac{\partial u_r}{\partial y}\right)^2},$$

$$A_4=2\overline{\left(\frac{\partial u_r}{\partial x}\right)^2}\Big/\overline{\left(\frac{\partial u_r}{\partial z}\right)^2},\quad A_5=2\overline{\left(\frac{\partial u_r}{\partial x}\right)^2}\Big/\overline{\left(\frac{\partial v_r}{\partial x}\right)^2},\quad A_6=2\overline{\left(\frac{\partial u_r}{\partial x}\right)^2}\Big/\overline{\left(\frac{\partial v_r}{\partial z}\right)^2},$$

$$A_7=2\overline{\left(\frac{\partial u_r}{\partial x}\right)^2}\Big/\overline{\left(\frac{\partial w_r}{\partial x}\right)^2},\quad A_8=2\overline{\left(\frac{\partial u_r}{\partial x}\right)^2}\Big/\overline{\left(\frac{\partial w_r}{\partial y}\right)^2},\quad A_9=-\frac{1}{2}\overline{\left(\frac{\partial u_r}{\partial x}\right)^2}\Big/\overline{\frac{\partial u_r}{\partial y}\frac{\partial v_r}{\partial x}},$$

$$A_{10}=-\frac{1}{2}\overline{\left(\frac{\partial u_r}{\partial x}\right)^2}\Big/\overline{\frac{\partial u_r}{\partial z}\frac{\partial w_r}{\partial x}},\quad A_{11}=-\frac{1}{2}\overline{\left(\frac{\partial u_r}{\partial x}\right)^2}\Big/\overline{\frac{\partial v_r}{\partial z}\frac{\partial w_r}{\partial y}}. \tag{3.5}$$

Local axisymmetry (George and Hussein, 1991) contains eight approximations with B_i = 1:

$$B_1=\overline{\left(\frac{\partial u_r}{\partial z}\right)^2}\Big/\overline{\left(\frac{\partial u_r}{\partial y}\right)^2},\quad B_2=\overline{\left(\frac{\partial v_r}{\partial x}\right)^2}\Big/\overline{\left(\frac{\partial w_r}{\partial x}\right)^2},\quad B_3=\overline{\left(\frac{\partial v_r}{\partial z}\right)^2}\Big/\overline{\left(\frac{\partial w_r}{\partial y}\right)^2},$$

$$B_4=\left[\frac{1}{3}\overline{\left(\frac{\partial u_r}{\partial x}\right)^2}+\frac{1}{3}\overline{\left(\frac{\partial v_r}{\partial z}\right)^2}\right]\Big/\overline{\left(\frac{\partial v_r}{\partial y}\right)^2},\quad B_5=\left[\frac{1}{3}\overline{\left(\frac{\partial u_r}{\partial x}\right)^2}+\frac{1}{3}\overline{\left(\frac{\partial v_r}{\partial z}\right)^2}\right]\Big/\overline{\left(\frac{\partial w_r}{\partial z}\right)^2},$$

$$B_6=\left[\frac{1}{6}\overline{\left(\frac{\partial u_r}{\partial x}\right)^2}-\frac{1}{3}\overline{\left(\frac{\partial v_r}{\partial z}\right)^2}\right]\Big/\overline{\frac{\partial v_r}{\partial z}\frac{\partial w_r}{\partial y}},\quad B_7=-\frac{1}{2}\overline{\left(\frac{\partial u_r}{\partial x}\right)^2}\Big/\overline{\frac{\partial u_r}{\partial y}\frac{\partial v_r}{\partial x}},$$

$$B_8=-\frac{1}{2}\overline{\left(\frac{\partial u_r}{\partial x}\right)^2}\Big/\overline{\frac{\partial u_r}{\partial z}\frac{\partial w_r}{\partial x}}. \tag{3.6}$$

Local homogeneity (Taylor, 1935) uses three approximations with $C_i = 1$:

$$C_1=-\overline{\left(\frac{\partial u_r}{\partial x}\right)^2}\Big/\left[\overline{\frac{\partial u_r}{\partial y}\frac{\partial v_r}{\partial x}}+\overline{\frac{\partial u_r}{\partial z}\frac{\partial w_r}{\partial x}}\right],\quad C_2=-\overline{\left(\frac{\partial v_r}{\partial y}\right)^2}\Big/\left[\overline{\frac{\partial u_r}{\partial y}\frac{\partial v_r}{\partial x}}+\overline{\frac{\partial v_r}{\partial z}\frac{\partial w_r}{\partial y}}\right],$$

$$C_3=-\overline{\left(\frac{\partial w_r}{\partial z}\right)^2}\Big/\left[\overline{\frac{\partial u_r}{\partial z}\frac{\partial w_r}{\partial x}}+\overline{\frac{\partial v_r}{\partial z}\frac{\partial w_r}{\partial y}}\right]. \tag{3.7}$$

Lastly, only one approximation is used for homogeneity in the *y*-*z* plane (Zhu and Antonia, 1997), i.e.:

$$D_1=\left[\overline{\left(\frac{\partial u_r}{\partial x}\right)^2}-2\overline{\frac{\partial v_r}{\partial z}\frac{\partial w_r}{\partial y}}\right]\Big/\left[\overline{\left(\frac{\partial v_r}{\partial y}\right)^2}+\overline{\left(\frac{\partial w_r}{\partial z}\right)^2}\right]=1. \tag{3.8}$$

Fig. 18 shows the transverse distributions of the ratios A_i, B_i, C_i and D_i at x/D = 10, 20, 40 and 100. The remainder component of the velocity ($\boldsymbol{u}_r$) is used for x/D = 10 and 20, because the coherent component is certainly not isotropic, axisymmetric or homogeneous. For x/D = 40 and 100, the total fluctuation component of the velocity ($\boldsymbol{u}'$) is used as a close representation of the remainder component, because the coherent component becomes negligible in the relatively far wake.

The validity of each approximation is revealed by a comparison with the ratio of 1 (marked by the horizontal dotted line in Fig. 18). With the increase in x/D from 10 to 100, the four sets of ratios A_i, B_i, C_i and D_i all show a gradual convergence towards 1, which suggests that the flow becomes increasingly isotropic, axisymmetric and homogeneous with distance downstream. However, the convergence efficiencies for the four sets of ratios are different.

For the surrogate of local isotropy, most of the ratios A_i deviate significantly from 1 over the entire wake (Fig. 18a–d). Even at x/D = 100, the deviations may be up to 30% (for the correlation terms A_9 and A_{11}), which suggests that local isotropy is not satisfied. Nevertheless, Fig. 18 confirms that all the ratios do fluctuate near 1. The fluctuations of $1/A_9 - 1/A_{11}$ and $1/B_6 - 1/B_8$ near 0 in Chen et al. (2018) are likely due to the difficulty in measuring the correlation terms accurately in physical experiments (Browne et al., 1987). Fig. 18(a–d) also shows that for $y/D \gtrsim 1$, the majority of the ratios A_i are smaller than 1, which explains why the surrogate $\varepsilon_{r,iso}$ under-predicts the

true ε_r (Fig. 17 and Fig. 16(e,f)).

For the surrogate of local axisymmetry, although $\varepsilon_{r,axis}$ matches well ε_r as early as $x/D = 20$ (Fig. 17b), individual ratios B_i still deviate noticeably from 1. Even at $x/D = 100$, the deviations may be up to 30% (for the correlation term B_7), which suggests that local axisymmetry is not satisfied. Nevertheless, a difference between A_i and B_i is that the B_i values are not biased significantly to either side of $B_i = 1$. Therefore, although local axisymmetry may not hold, the deviations of the B_i values from $B_i = 1$ may be largely cancelled out and result in a good match between $\varepsilon_{r,axis}$ and ε_r for $x/D \geq 20$.

For the surrogates of local homogeneity and homogeneity in the y-z plane, the results shown in Fig. 18(i–p) suggest that the good performances of $\varepsilon_{r,hom}$ and $\varepsilon_{r,yz}$ are indeed due to the general validity of $C_i = 1$ and $D_i = 1$, i.e. the turbulent dissipation is indeed largely locally homogeneous. Although noticeable deviations of C_i and D_i from 1 are observed at $x/D = 10$ and $y/D \gtrsim 2$ (Fig. 18i,m), their influence on the performance of $\varepsilon_{r,hom}$ and $\varepsilon_{r,yz}$ is minor, because (i) at $x/D = 10$ and $y/D \gtrsim 2$, the ε_r value itself is relatively small (Fig. 17), and (ii) for the surrogates $\varepsilon_{r,hom}$ and $\varepsilon_{r,yz}$, only three or two out of the twelve velocity derivative terms are unmeasured, such that the influence on the overall $\varepsilon_{r,hom}$ and $\varepsilon_{r,yz}$ values is minor.

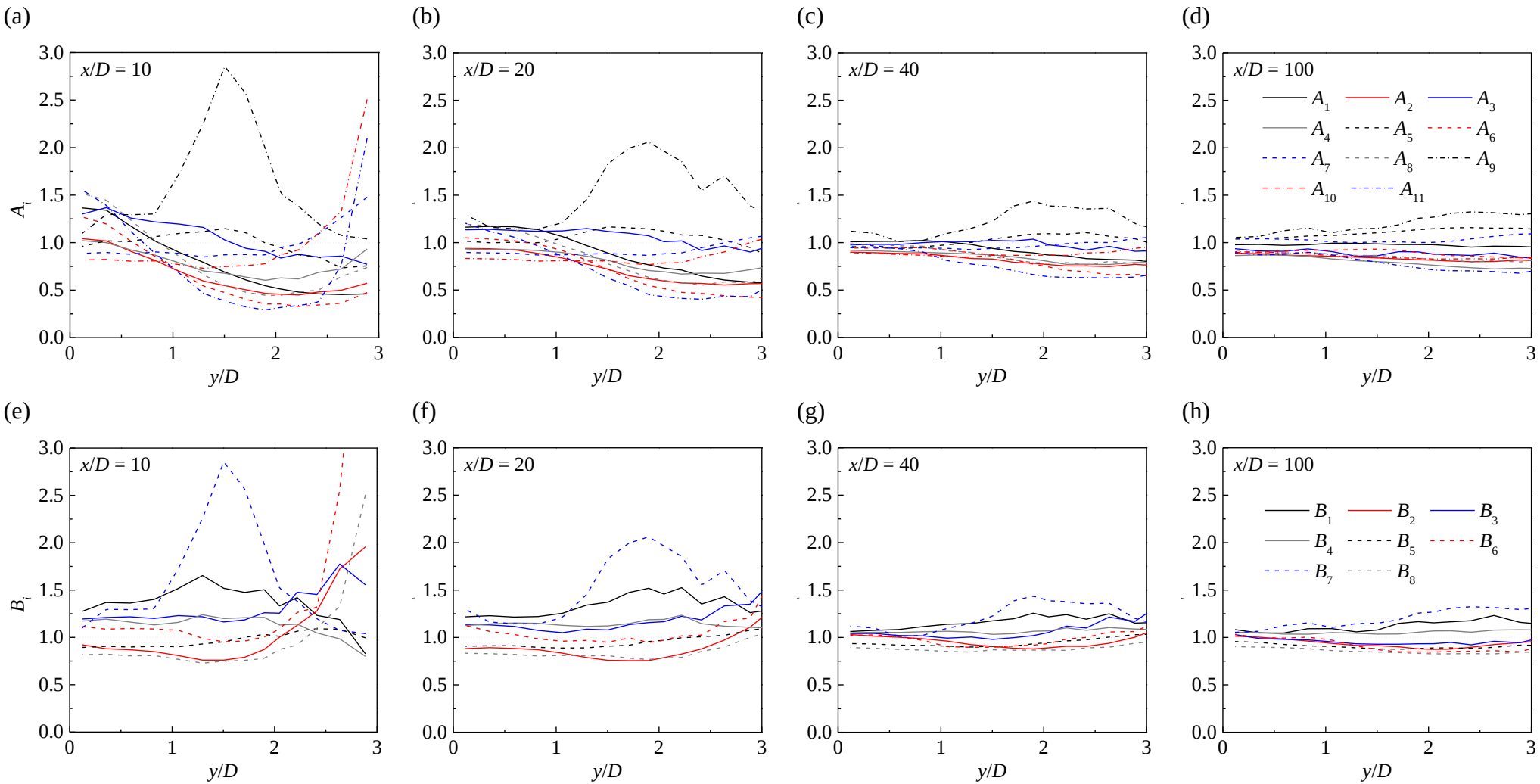
(a)
(b)
(c)
(d)
(e)
(f)
(g)
(h)
x/D = 10
x/D = 20
x/D = 40
x/D = 100
A_i
B_i
y/D
A1 A2 A3 A4 A5 A6 A7 A8 A9 A10 A11
B1 B2 B3 B4 B5 B6 B7 B8

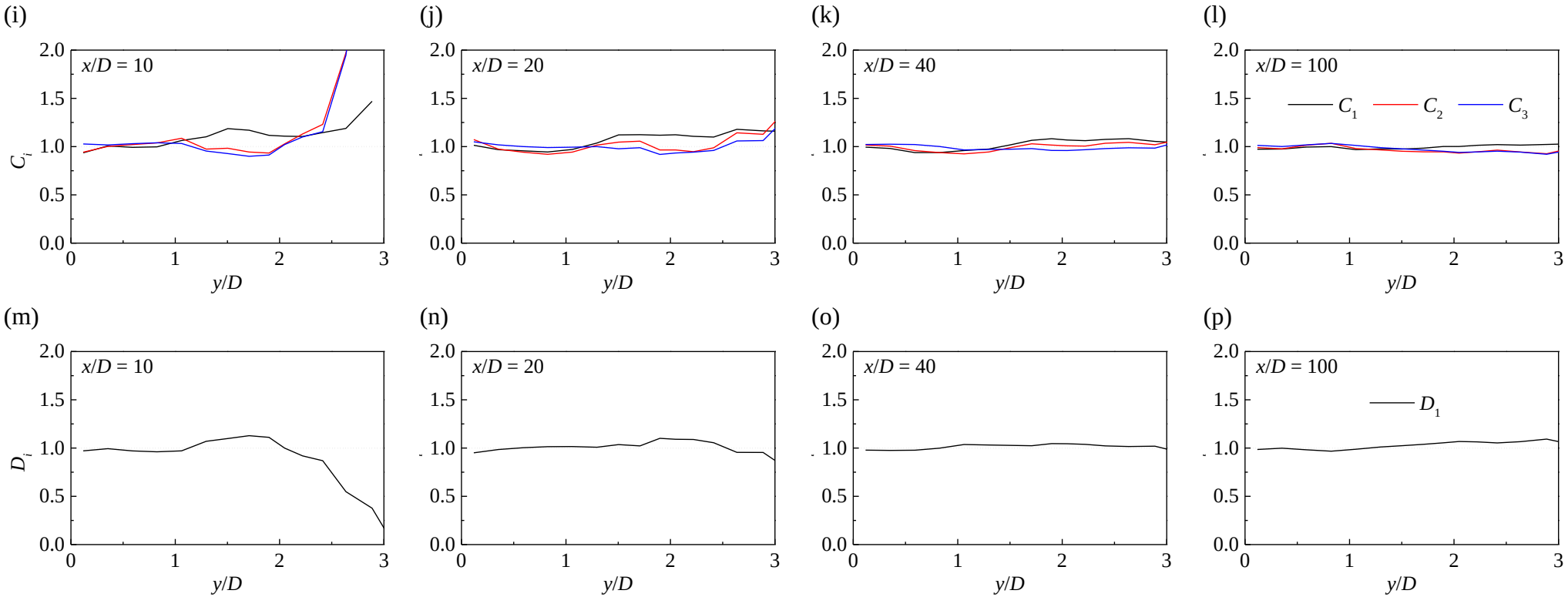

Fig. 18. Individual examination of the ratios A_i, B_i, C_i and D_i: (a) A_i at x/D = 10, (b) A_i at x/D = 20, (c) A_i at x/D = 40, (d) A_i at x/D = 100, (e) B_i at x/D = 10, (f) B_i at x/D = 20, (g) B_i at x/D = 40, (h) B_i at x/D = 100, (i) C_i at x/D = 10, (j) C_i at x/D = 20, (k) C_i at x/D = 40, (l) C_i at x/D = 100, (m) D_i at x/D = 10, (n) D_i at x/D = 20, (o) D_i at x/D = 40, and (p) D_i at x/D = 100. The horizontal dotted line in each panel highlights the ratio of 1.

3.7. Turbulent kinetic energy

In addition to the velocity derivative terms, the anisotropic nature of the turbulent wake is also revealed by the turbulent kinetic energy. Fig. 19 shows the transverse distributions of the three energy components sampled at x/D = 10, 20, 60 and 100. The kinetic energy is calculated based on the total velocity fluctuation. To facilitate examination of the anisotropy, the averaged value, i.e. $\left(\overline{u'u'}+\overline{v'v'}+\overline{w'w'}\right)\Big/\left(3U^2\right)$, is also plotted in Fig. 19. For x/D = 10 and 20, the three energy components deviate significantly from the averaged value, owing to the noticeable contribution of the coherent structures (Fig. 4) to the kinetic energy at x/D = 10 and 20. The coherent and remainder components of the kinetic energy are separated in Fig. 20, based on the phase average using the reference signals at the corresponding x/D. The percentage contribution (α) of the coherent component, which is calculated as

$$\alpha = \frac{\int\left(\tilde{\overline{u}}\tilde{\overline{u}}+\tilde{\overline{v}}\tilde{\overline{v}}+\tilde{\overline{w}}\tilde{\overline{w}}\right)\mathrm{d}y}{\int\left(\overline{u'u'}+\overline{v'v'}+\overline{w'w'}\right)\mathrm{d}y}\times 100\%, \tag{3.9}$$

is 38.2% at x/D = 10 and 17.1% at x/D = 20. Because the coherent component induced by the primary vortex street is apparently anisotropic (Fig. 20a,c), after removing this component the remainder component displays an improved degree of isotropy (Fig. 20b,d). Nevertheless, moderate deviations from the averaged value still exist. The anisotropic nature of the wake is also observed further downstream at e.g. x/D = 60 and 100 (Fig. 19c,d). At x/D = 60 and 100, the coherent component induced by the primary vortex street is expected to be negligible (e.g. section 3.2 shows that the frequency peak at *St* disappears at x/D = 64), such that the remainder component is approximated by the total fluctuation component. Fig. 19(c,d) suggests that even after the annihilation of the primary vortex street, the turbulence in the wake is still globally anisotropic and non-axisymmetric.

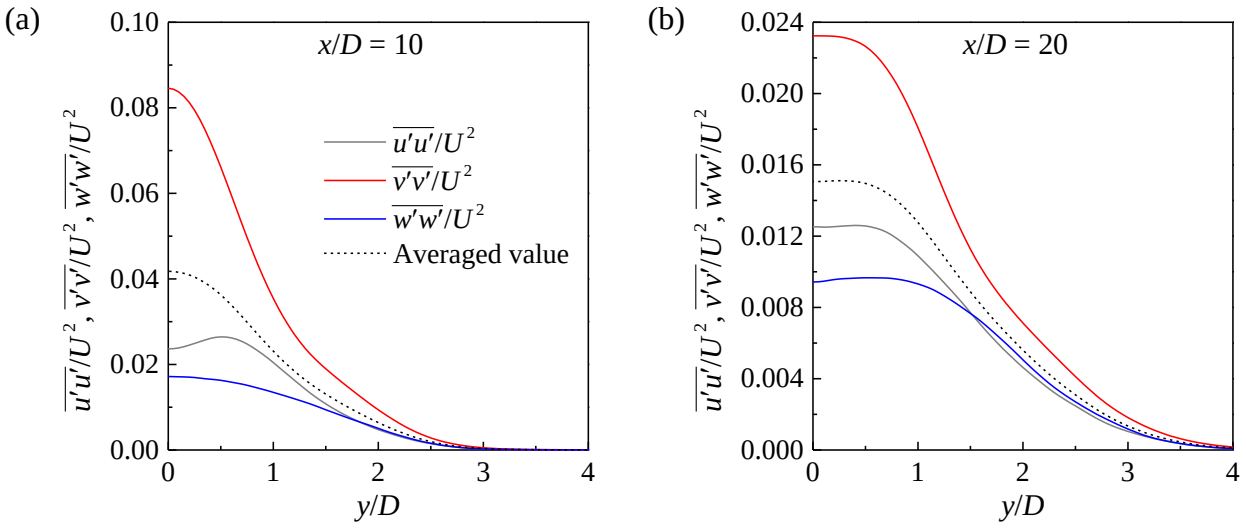

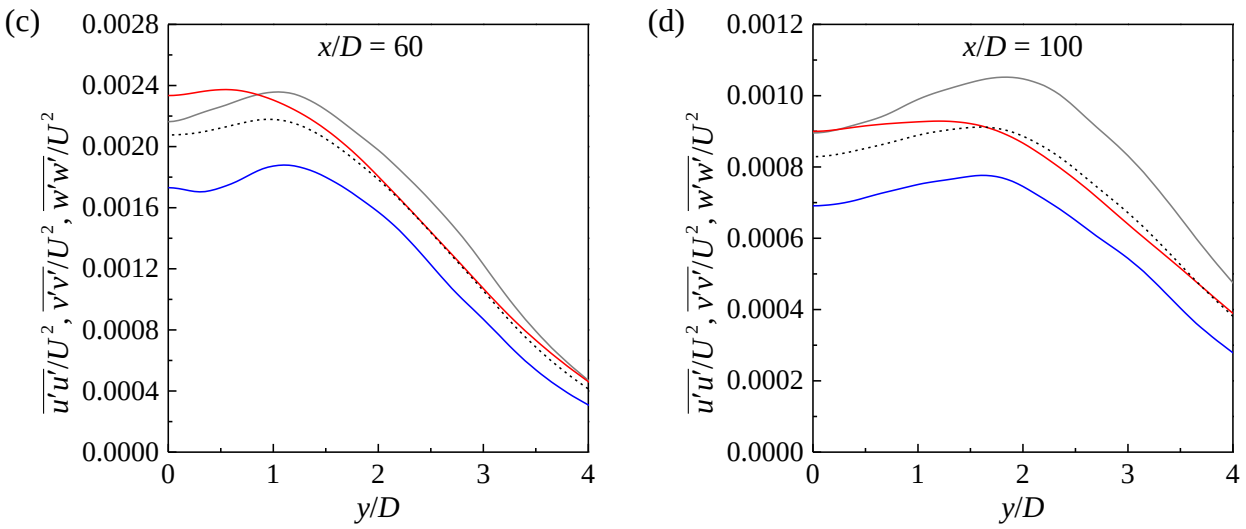

Fig. 19. Transverse distributions of the three components of the kinetic energy (based on the total fluctuation component of the velocity) at (a) x/D = 10, (b) x/D = 20, (c) x/D = 60, and (d) x/D = 100.

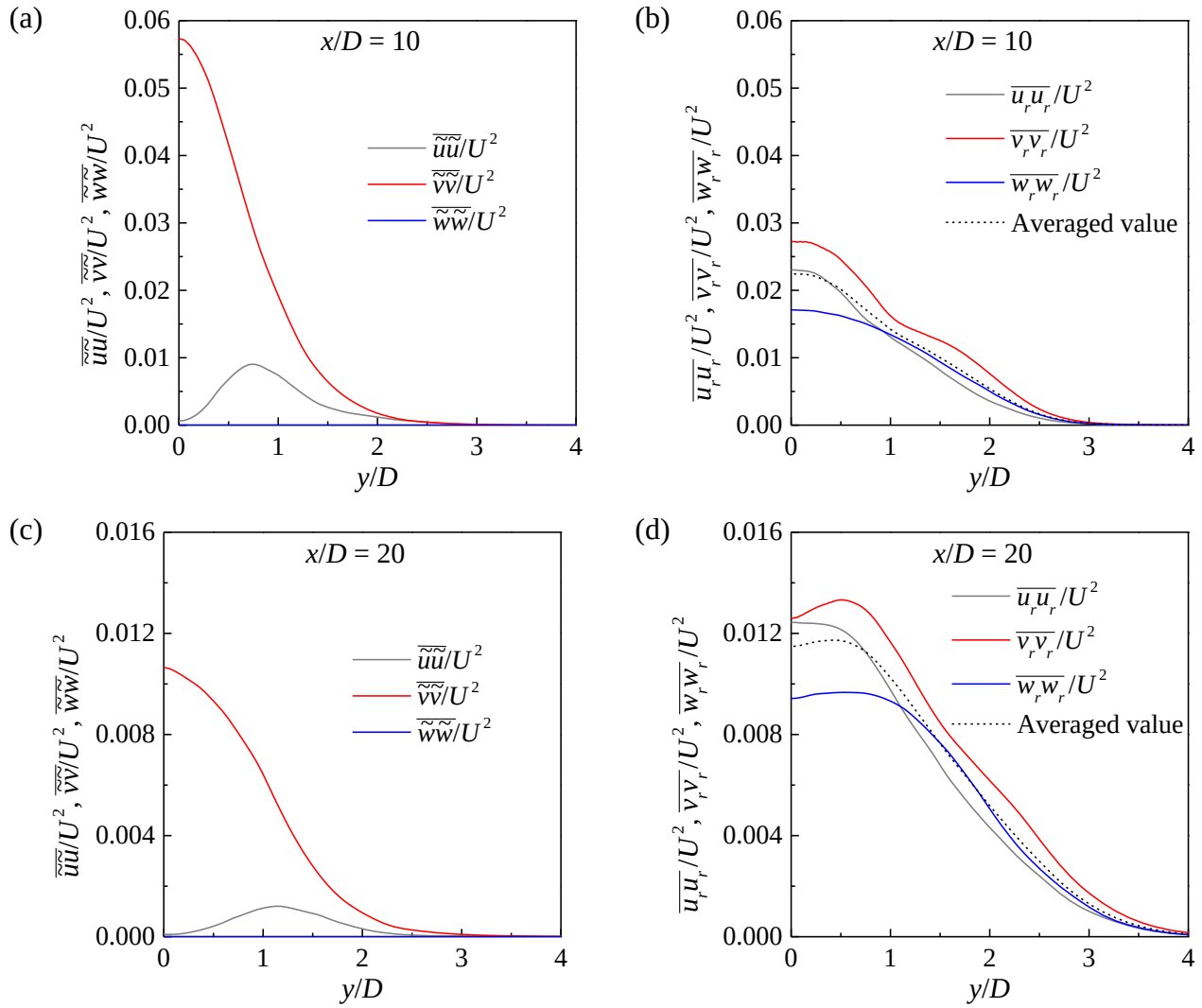

Fig. 20. Transverse distributions of the three components of the kinetic energy at (a)

x/D = 10 (coherent component), (b) x/D = 10 (remainder component), (c) x/D = 20 (coherent component), and (d) x/D = 20 (remainder component).

Among the three energy components $\overline{u_r u_r}$, $\overline{v_r v_r}$ and $\overline{w_r w_r}$, the dominant component changes from $\overline{v_r v_r}$ for the relatively near wake (e.g. x/D = 10 and 20 shown in Fig. 20(b,d)) to $\overline{u_r u_r}$ for the relatively far wake (e.g. x/D = 100 shown in Fig. 19(d)). Fig. 21 quantifies the relative strength/contribution of the three energy components at x/D = 10, 20, 60 and 100, where E_x, E_y, E_z and E are calculated as

$$E_x = \frac{1}{2}\int \frac{\overline{u_r u_r}}{U^2}\,\mathrm{d}\left(\frac{y}{D}\right), \tag{3.10}$$

$$E_y = \frac{1}{2}\int \frac{\overline{v_r v_r}}{U^2}\,\mathrm{d}\left(\frac{y}{D}\right), \tag{3.11}$$

$$E_z = \frac{1}{2}\int \frac{\overline{w_r w_r}}{U^2}\,\mathrm{d}\left(\frac{y}{D}\right), \tag{3.12}$$

$$E = E_x + E_y + E_z . \tag{3.13}$$

The dominance of E_y over E_x and E_z in the relatively near wake is likely due to the influence of the primary vortex street. With an increase of x/D into the relatively far wake, E_x gradually takes over E_y to be the dominant component, i.e. the turbulent kinetic energy is preferred to reside in the streamwise direction. Chen et al. (2016) also observed a dominance of the $\overline{u'u'}$ component at x/D = 40 of the turbulent wake at Re = 2500, and attributed this phenomenon to the dominance of the strong mean flow in the streamwise direction. Furthermore, Zhou and Antonia (2000) showed that in the turbulent wake generated by a grid (without large-scale coherent primary vortices which develop in the wake of a cylinder), the $\overline{u'u'}$ component in the direction of the mean flow was also noticeably larger than the $\overline{v'v'}$ component.

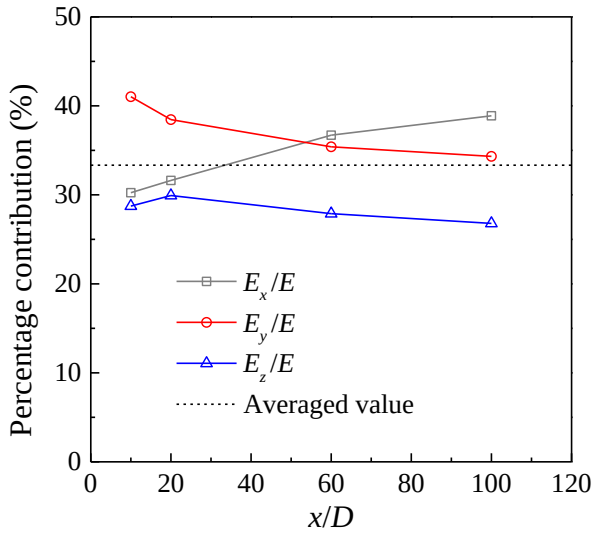

Fig. 21. Percentage contribution of the three energy components at various x/D.

3.8. Phase-averaged turbulence characteristics

In addition to the time-averaged turbulence characteristics examined in sections 3.3 to 3.7, this section examines the phase-averaged turbulence characteristics. The present results serve as a first numerical validation of the phase-averaged turbulence characteristics observed experimentally by e.g. Cantwell and Coles (1983), Hussain and Hayakawa (1987) and Chen et al. (2018). In the physical experiments by Hussain and Hayakawa (1987) and Chen et al. (2018), the measurements were taken at discrete streamwise locations, such that the phase-averaged turbulence characteristics were reported in the φ–y space. In contrast, the present numerical results are presented in the x–y space.

In Fig. 22, the phase- and span-averaged turbulence characteristics are illustrated at a phase when the C_L signal reaches its maximum. Although the phase- and span-averaging based on the C_L signal obtained at $x/D \sim 0$ may result in moderate under-prediction of the phase-averaged wake characteristics at further downstream locations (e.g. an under-prediction of the peak vorticity of the primary vortices at x/D = 10 and 20 in Fig. 5(d)), qualitatively the spatial distributions of different phase-averaged turbulence characteristics can still be revealed and compared.

Fig. 22(a) shows the spatial distribution of the phase-averaged spanwise vorticity $\langle \omega_z \rangle$. The vortex centres are identified by the location of peak vorticity within each primary vortex, and are marked by solid dots in each panel of Fig. 22. Fig. 22(b) shows the spatial distribution of the two-dimensional (2D) turbulence production $\langle P \rangle$, where $\langle P \rangle$ is defined as (Cantwell and Coles, 1983; Hussain and Hayakawa, 1987)

$$\langle P \rangle = -\langle u_{i,r} u_{j,r} \rangle \frac{\partial \langle u_i \rangle}{\partial x_j} \qquad (i, j = 1, 2). \tag{3.14}$$

The location of peak $\langle P \rangle$ within each production region is marked by an open circle. A comparison between Fig. 22(a) and Fig. 22(b) suggests that the regions of primary vortices and 2D turbulence production follow staggered spatial distributions, which agrees with the conceptual model proposed by Hussain and Hayakawa (1987).

Fig. 22(c,d) decomposes the dissipation rate into that contributed by the mean flow and coherent primary vortices $\langle \varepsilon_m + \tilde{\varepsilon} \rangle$ (Fig. 22c) and that contributed by the remainder $\langle \varepsilon_r \rangle$ (Fig. 22d), where the former coincides with the regions of turbulence production, whereas the latter mainly resides within the regions of primary vortices. In Chen et al.'s (2018) physical experiments, they conducted flow measurements at discrete streamwise locations, and reported similar features in the φ–y space. The present numerical results serve as a confirmation of these features in an alternative x–y space.

Fig. 22(e,f) decomposes the kinetic energy into that contributed by the coherent primary vortices $\langle (\tilde{u}\tilde{u} + \tilde{v}\tilde{v})/2 \rangle$ (Fig. 22e) and that contributed by the remainder $\langle (u_r u_r + v_r v_r + w_r w_r)/2 \rangle$ (Fig. 22f). The coherent component does not coincide with either the primary vortices or turbulence production. Fig. 23(a,b) further decomposes the coherent component into $\langle \tilde{u}\tilde{u}/2 \rangle$ and $\langle \tilde{v}\tilde{v}/2 \rangle$, where the former peaks symmetrically away from the centreline, while the latter peaks near the centreline. In contrast, the remainder component shown in Fig. 22(f) mainly resides within the regions of primary vortices. Hussain and Hayakawa (1987) also showed that the 2D remainder component $\langle (u_r u_r + v_r v_r)/2 \rangle$ agreed well with the regions of primary vortices. The present 3D results further confirm that $\langle u_r u_r/2 \rangle$, $\langle v_r v_r/2 \rangle$ and $\langle w_r w_r/2 \rangle$ all peak within the regions of primary vortices (Fig. 23c–e).

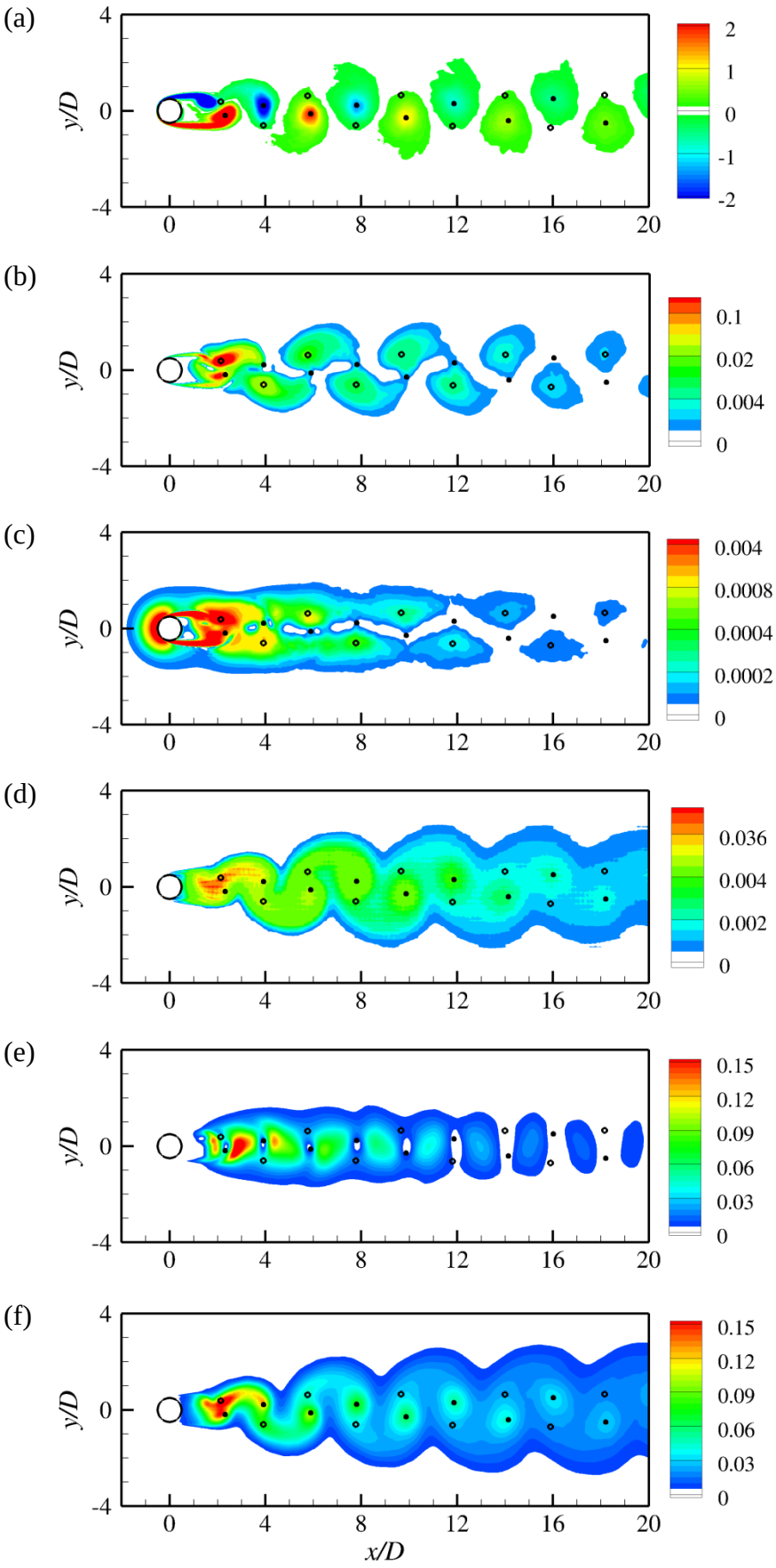

Fig. 22. Phase- and span-averaged turbulence characteristics in the wake of a circular

cylinder at *Re* = 1000: (a) spanwise vorticity $\langle \omega_z \rangle$, (b) 2D turbulence production $\langle P \rangle$, (c) dissipation rate contributed by the mean flow and coherent primary vortices $\langle \varepsilon_m + \tilde{\varepsilon} \rangle$, (d) dissipation rate contributed by the remainder $\langle \varepsilon_r \rangle$, (e) kinetic energy contributed by the coherent primary vortices $\langle (\tilde{u}\tilde{u} + \tilde{v}\tilde{v})/2 \rangle$, and (f) kinetic energy contributed by the remainder $\langle (u_r u_r + v_r v_r + w_r w_r)/2 \rangle$. The turbulence characteristics are shown at a phase when the C_L signal reaches its maximum. The locations of peak $\langle \omega_z \rangle$ and $\langle P \rangle$ are marked by solid and open circles, respectively. All the quantities have been normalised by *U* and *D*.

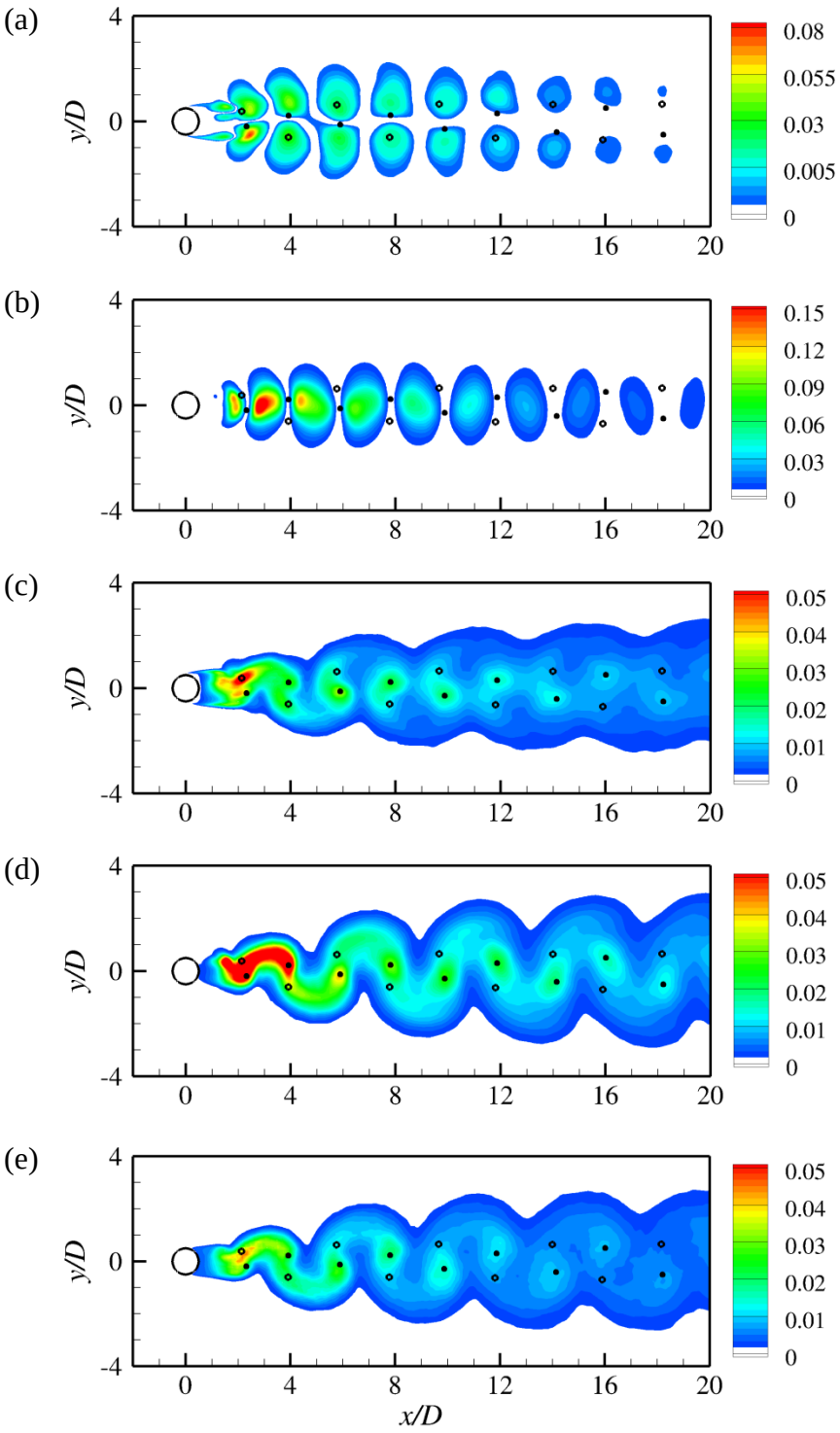

Fig. 23. Phase- and span-averaged kinetic energy components in the wake of a circular cylinder at *Re* = 1000: (a) $\langle \tilde{u}\tilde{u}/2 \rangle$, (b) $\langle \tilde{v}\tilde{v}/2 \rangle$, (c) $\langle u_r u_r/2 \rangle$, (d) $\langle v_r v_r/2 \rangle$, and (e) $\langle w_r w_r/2 \rangle$. The turbulence characteristics are shown at a phase when the C_L signal reaches its maximum. The locations of peak $\langle \omega_z \rangle$ and $\langle P \rangle$ are marked by solid and open circles, respectively. All the quantities have been normalised by *U*.

Among the turbulence characteristics shown in Fig. 22, the ω_z, P, $\varepsilon_m + \tilde{\varepsilon}$ and $(\tilde{u}\tilde{u} + \tilde{v}\tilde{v})/2$ fields are nominally 2D. In contrast, the ε_r and $(u_r u_r + v_r v_r + w_r w_r)/2$ fields may contain intrinsic 3D structures, and their spatial distributions relative to the 3D vortex structures are examined. Fig. 24 illustrates an instantaneous 3D flow field at the same phase to that shown in Fig. 22. In both Fig. 24(a) and Fig. 22(a), several spanwise vortex rollers are observed at x/D ~ 2.3, 3.9 and 5.9. Fig. 24(b) shows the spanwise distribution of the streamwise vortices. A comparison between Fig. 24(c,d) and Fig. 24(b) suggests that the spanwise distributions of the streamwise structures of ε_r and $(u_r u_r + v_r v_r + w_r w_r)/2$ follow closely the spanwise distribution of the streamwise vortices, which further suggests that the remainder component of the dissipation rate and kinetic energy not only resides within the regions of primary vortices (as shown in Fig. 22(d,f)), but also follows closely the regions of streamwise vortices. This feature is also reflected by the fact that the phase-averaged $\langle \varepsilon_r \rangle$ and $\langle (u_r u_r + v_r v_r + w_r w_r)/2 \rangle$ fields do not solely occupy the regions of primary vortices, but also fill the braid regions between the primary vortices (Fig. 22d,f), which signifies the contribution from the streamwise vortices.

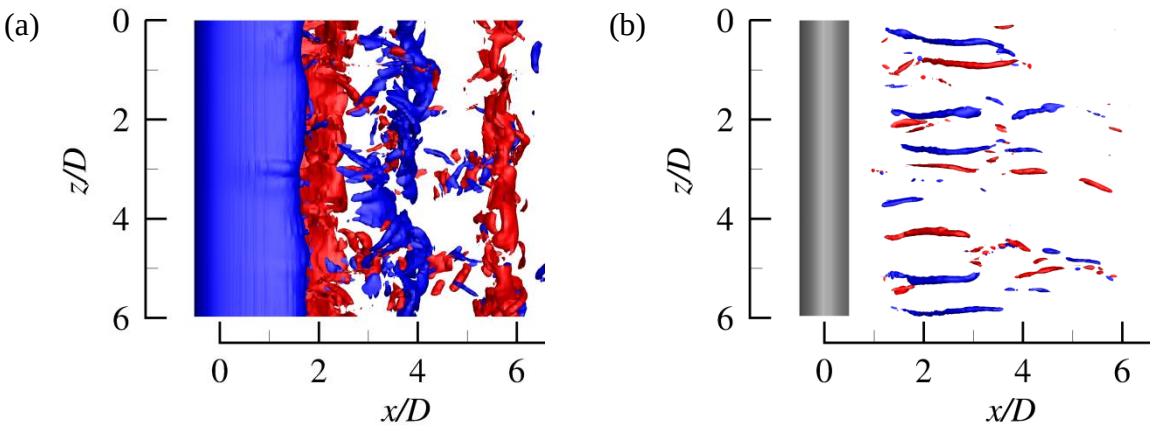

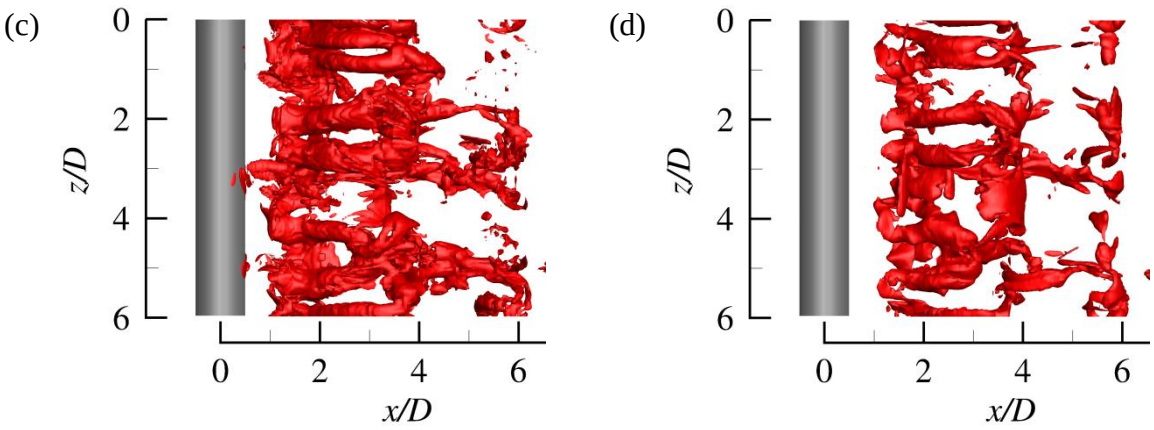

Fig. 24. Instantaneous turbulence characteristics in the wake of a circular cylinder at *Re* = 1000: (a) spanwise vorticity $\omega_z = \pm 4$, (b) streamwise vorticity $\omega_x = \pm 12$, (c) remainder component of the dissipation rate $\varepsilon_r = 0.03$, and (d) remainder component of the kinetic energy $\left(u_r u_r + v_r v_r + w_r w_r\right)/2 = 0.15$. The turbulence characteristics are shown at a phase when the C_L signal reaches a local maximum. All the quantities have been normalised by *U* and *D*.

4. Conclusions

This study examines the primary vortex street, turbulent kinetic energy and energy dissipation rate in the wake of a circular cylinder at *Re* = 1000. In the turbulent near to intermediate wake, the primary vortex street gradually decays with distance downstream and is annihilated at *x*/*D* ~ 64. The spatial distribution of the primary and streamwise vortices dictates the spatial distribution of the turbulence characteristics. Based on the present high-fidelity DNS data, the full kinetic energy dissipation rate in the wake (up to *x*/*D* = 120) is quantified based on the determination of all twelve velocity derivative terms, including the three correlation terms that are difficult to be measured accurately by physical experiments.

The total dissipation rate ε is decomposed into the contributions from the mean flow, the coherent primary vortices and the remainder (denoted ε_m, $\tilde{\varepsilon}$ and ε_r, respectively). Because at a specific *x*/*D* the three components may peak at different transverse locations, the percentage contribution of each component is quantified through integrating the corresponding component along the *y*-direction. The ε_m component, which is associated with the mean shear around the cylinder, dominates the immediate neighbourhood of the cylinder but contributes merely ~ 1% to the total ε at *x*/*D* > 4. The $\tilde{\varepsilon}$ component, which is associated with the coherent primary vortices, accounts for 4.2% and 2.0% of the total ε at *x*/*D* = 10 and 20, respectively. The ε_r component, which occurs only in the 3D turbulent wake, accounts for the majority of the total ε for almost the entire wake (beyond the immediate neighbourhood of the cylinder), e.g. 95% and 97% for *x*/*D* = 10 and 20, respectively.

As a comparison, the turbulent kinetic energy is 62% and 83% contributed by the remainder component at x/D = 10 and 20, respectively.

Based on the ε_r component, the validity of local isotropy, local axisymmetry, local homogeneity and homogeneity in the y-z plane for the turbulent dissipation in the wake is examined. Based on individual examinations of the approximations for the unmeasured velocity derivative terms, it is found that the turbulent dissipation (examined up to x/D = 120) is largely locally homogeneous, but not locally isotropic or axisymmetric, even after the annihilation of the primary vortex street. In addition, an analysis of the turbulent kinetic energy in the wake suggests that globally the turbulence in the wake is also anisotropic and non-axisymmetric.

With the availability of the full DNS data, the performances of the four surrogates to the true dissipation rate are evaluated. When considering the ε' component of the dissipation rate, the surrogates ε'_{yz}, ε'_{hom} and ε'_{axis} agree well with ε' for $x/D \gtrsim 5$, 20 and 40, respectively, while ε'_{iso} does not match ε' for the entire wake. When considering the ε_r component, improved performances are observed for $\varepsilon_{r,hom}$ and $\varepsilon_{r,axis}$ at e.g. x/D = 10 and 20. The improved performances arise from the removal of the $\tilde{\varepsilon}$ component, since the $\tilde{\varepsilon}$ component is by no means isotropic, axisymmetric or homogeneous.

Physically, the good performances of $\varepsilon_{r,hom}$ and $\varepsilon_{r,yz}$ are indeed due to the general validity of local homogeneity for the turbulent dissipation. Although local axisymmetry does not hold, errors induced by the approximations for the unmeasured velocity derivative terms largely cancel out, which leads to a good performance of the surrogate $\varepsilon_{r,axis}$ as a whole. For local isotropy, however, most of the unmeasured velocity derivative terms are under-predicted by the approximations (mainly for $y/D \gtrsim 1$), such that $\varepsilon_{r,iso}$ under-predicts the true ε_r.

Acknowledgments

The first author would like to acknowledge the support from the Australian Research Council through the DECRA scheme (Grant No. DE190100870). The authors would also like to acknowledge the help from Dr. Xiaoying Ju in data processing. This work was supported by resources provided by the Pawsey Supercomputing Centre and the National Computational Infrastructure with funding from the Australian Government and the Government of Western Australia.

Declaration of interests

The authors report no conflict of interest.

Appendix A. Numerical validation of $\varepsilon = \varepsilon_m + \tilde{\varepsilon} + \varepsilon_r$

A numerical validation of the relationship $\varepsilon = \varepsilon_m + \tilde{\varepsilon} + \varepsilon_r$ was performed based on the reference case/mesh introduced in section 2.2. The time history of the lift

coefficient (C_L) on the cylinder was used as a reference signal for selecting 16 phases ($\varphi = n\times(2\pi/16)$, where n is an integer from 0 to 15; see section 2.3) over each vortex shedding period T. The statistical time period was $50T$, i.e. a total of $16\times50 = 800$ instantaneous flow fields were used for the analysis. Although a time period of $50T$ may not be long enough for obtaining a statistically stationary dissipation rate, the numerical validation of $\varepsilon = \varepsilon_m + \tilde{\varepsilon} + \varepsilon_r$ was unaffected by the statistical length, since an identical statistical length was used for all four terms.

For each instantaneous flow field, the total velocity field $\boldsymbol{u}$ was decomposed into

$$\boldsymbol{u} = \boldsymbol{u}_m + \tilde{\boldsymbol{u}} + \boldsymbol{u}_r . \tag{A.1}$$

Based on the 800 instantaneous $\boldsymbol{u}$ fields, one $\boldsymbol{u}_m$ field, 16 different $\tilde{\boldsymbol{u}}$ fields and 800 instantaneous $\boldsymbol{u}_r$ fields, the corresponding ε, ε_m, $\tilde{\varepsilon}$ and ε_r fields were determined by equations (1.5)–(1.8). Fig. 25 shows the transverse distributions of different components of the mean dissipation rate at x/D = 5 and 10. The numerical results demonstrated the validity of $\varepsilon = \varepsilon_m + \tilde{\varepsilon} + \varepsilon_r$. Although the use of the time history of C_L (at $x/D \sim 0$) as the reference signal for phase average may slightly underestimate the coherent component $\tilde{\varepsilon}$ and overestimate the remainder ε_r at x/D = 5 and 10, it is irrelevant to the demonstration presented herein.

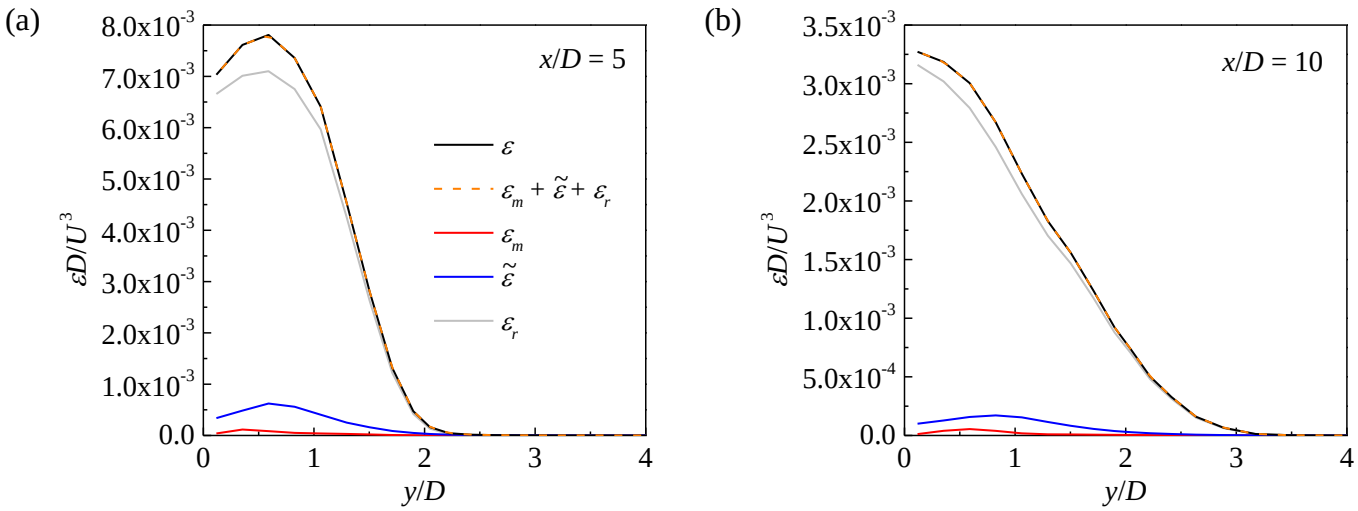

Fig. 25. Transverse distributions of different components of the mean kinetic energy dissipation rate at (a) x/D = 5, and (b) x/D = 10.

Appendix B. Mesh convergence

A detailed convergence check for the reference mesh introduced in section 2.2 is reported below. Firstly, the mesh resolution near the cylinder was examined via a p-type refinement through varying the N_p value from 4 to 3 and 5. The time-step size was modified accordingly (Table 2) so as to satisfy the CFL limit of approximately 0.5. The corresponding numerical results are listed in Table 2. The Strouhal number

(St), drag and lift coefficients (C_D and C_L), root-mean-square lift coefficient ($C_{L,rms}$) and base pressure coefficient (C_{pb}) are calculated as:

$$St = \frac{f_L D}{U}, \tag{B.1}$$

$$C_D = \frac{F_D}{\frac{1}{2}U^2 D L_z}, \tag{B.2}$$

$$C_L = \frac{F_L}{\frac{1}{2}U^2 D L_z}, \tag{B.3}$$

$$C_{L,rms} = \sqrt{\frac{1}{N}\sum_{i=1}^{N}\left(C_{L,i} - \overline{C_L}\right)^2}, \tag{B.4}$$

$$C_{pb} = \frac{p_b - p_\infty}{\frac{1}{2}U^2}, \tag{B.5}$$

where f_L is the peak frequency obtained from the fast Fourier transform (FFT) of the time history of C_L, F_D and F_L are the drag and lift forces on the cylinder (which have been divided by the fluid density), respectively, $\overline{C_D}$ and $\overline{C_L}$ denote time-averaged drag and lift coefficients, respectively, N is the data length of the time history of C_L, p_b is the time-averaged kinematic pressure at the rear point of the cylinder, and p_∞ is the reference at the inlet boundary. The wake recirculation length (L_r) is the horizontal distance between the rear point of the cylinder and the downstream end of the time-averaged wake recirculation zone.

Table 2. Convergence check of the mesh resolution near the cylinder for Re = 1000. The DNS results of Jiang and Cheng (2017) are from the case with the highest mesh resolution. The experimental results include St from Norberg (2003), $\overline{C_D}$ from Wieselsberger (1922), $C_{L,rms}$ from Norberg (2003), C_{pb} from Norberg (1994) and Williamson and Roshko (1990), and L_r from Noca et al. (1998).

Case description	Δt^*	St	$\overline{C_D}$	$C_{L,rms}$	$-C_{pb}$	L_r/D
N_p = 3,	0.005	0.2101	0.985	0.079	0.795	1.697
N_p = 4 (reference)	0.003125	0.2103	0.994	0.091	0.807	1.651
N_p = 5	0.002	0.2105	0.995	0.093	0.806	1.637
N_p = 5, another 600 time units	0.002	0.2102	0.999	0.097	0.812	1.622
Jiang and Cheng (2017)		0.2106	1.000	0.100	0.815	1.612
Experimental result		0.210	0.98	0.058	0.81	1.65

As shown in Table 2, the variations in the numerical results with N_p = 3–5 were rather small, which suggested that even the relatively coarse mesh with N_p = 3 was largely adequate in predicting the flow characteristics near the cylinder. To rule out

the influence of the numerical set-up (which was based on the framework of Nektar++), cross-checks were performed based on the DNS results obtained with a different open-source code OpenFOAM (www.openfoam.org) which was based on the conventional finite volume method. Details of the numerical schemes and mesh convergence for the OpenFOAM model can be found in Jiang and Cheng (2017), and the numerical results based on the highest mesh resolution used by Jiang and Cheng (2017) are listed in Table 2. Table 2 also summarises some experimental results reported in the literature (Norberg, 2003; Wieselsberger, 1922; Norberg, 1994; Williamson and Roshko, 1990; Noca et al., 1998). The present numerical results agreed well with the DNS results reported by Jiang and Cheng (2017) and the experimental results listed in Table 2.

Secondly, the mesh resolution in the relatively far wake was examined by a convergence check of the mean kinetic energy dissipation rate ε. The macro-element mesh shown in Fig. 2 (with a constant streamwise size of $\Delta x = 0.2D$ for x/D = 4–120) was tested with N_p = 3, 4 and 5. In addition, it is also of interest to examine the effect of element stretching in the wake on the numerical results. Therefore, a modified macro-element mesh, where the streamwise size of the macro-elements stretched linearly from $\Delta x = 0.2D$ at x/D = 4 to $1.05D$ at x/D = 120, was also tested with N_p = 3, 4 and 5. The expansion ratio of Δx from x/D = 4 to 120, i.e. 1.05/0.2 = 5.25, was selected based on the expansion ratio of the Kolmogorov length scale (η) in the wake, which was 5.23 over the same range of x/D (shown later on in Fig. 31(a)), such that the ratio between the streamwise cell size ($\Delta x/N_p$) and η remained nearly constant over x/D = 4–120 (e.g. $(\Delta x/N_p)/\eta \sim 2.85$ when N_p = 4). The modified macro-element mesh contained 12,054 elements (cf. 26,922 for the reference mesh), such that for each N_p value, the computational cost was approximately 1/3 of that for the corresponding case without element stretching (Table 3).

Table 3. Computational details for the test cases examining the far-wake resolution.

Case description		Δt*	Cores	Core hours for 1000 time units
Constant Δx	N_p = 5	0.002	5×24	196,000
	N_p = 4 (ref)	0.003125	5×24	82,000
	N_p = 3	0.005	4×24	35,000
Stretched Δx	N_p = 5	0.002	3×24	64,000
	N_p = 4	0.003125	2×24	27,000
	N_p = 3	0.005	2×24	12,000

Fig. 26 shows the transverse distribution of the mean kinetic energy dissipation rate at x/D = 10, 20, 50 and 100. In addition to the time average, the results were also averaged along the spanwise direction and between the two sides of the wake centreline. For both types of the macro-element meshes (with and without stretched Δx in the wake), the predicted dissipation rate converged towards increased values with increasing N_p. For the macro-element mesh without stretching, the dissipation rate largely converged at $N_p \geq 4$. For the macro-element mesh with stretching,

however, the convergence rate was slower (especially at relatively large x/D values, where the dissipation rate predicted with N_p = 5 was similar to that predicted by the mesh without stretching with N_p = 4, because Δx was increasingly stretched with distance downstream). A similar convergence performance was also observed for a typical term $\overline{(\partial u/\partial x)^2}$ for the dissipation rate (Fig. 27). Nevertheless, owing to the reduced number of macro-elements used in the stretched mesh, the computational cost for the case with stretched Δx and N_p = 5 was similar to that for the case with constant Δx and N_p = 4 (Table 3). In consideration of a larger-scale parallel computation for the latter case (Table 3), as well as a compromise between numerical accuracy and computational cost, the case with constant Δx and N_p = 4 (the reference case introduced in section 2.2) was adopted for the present study.

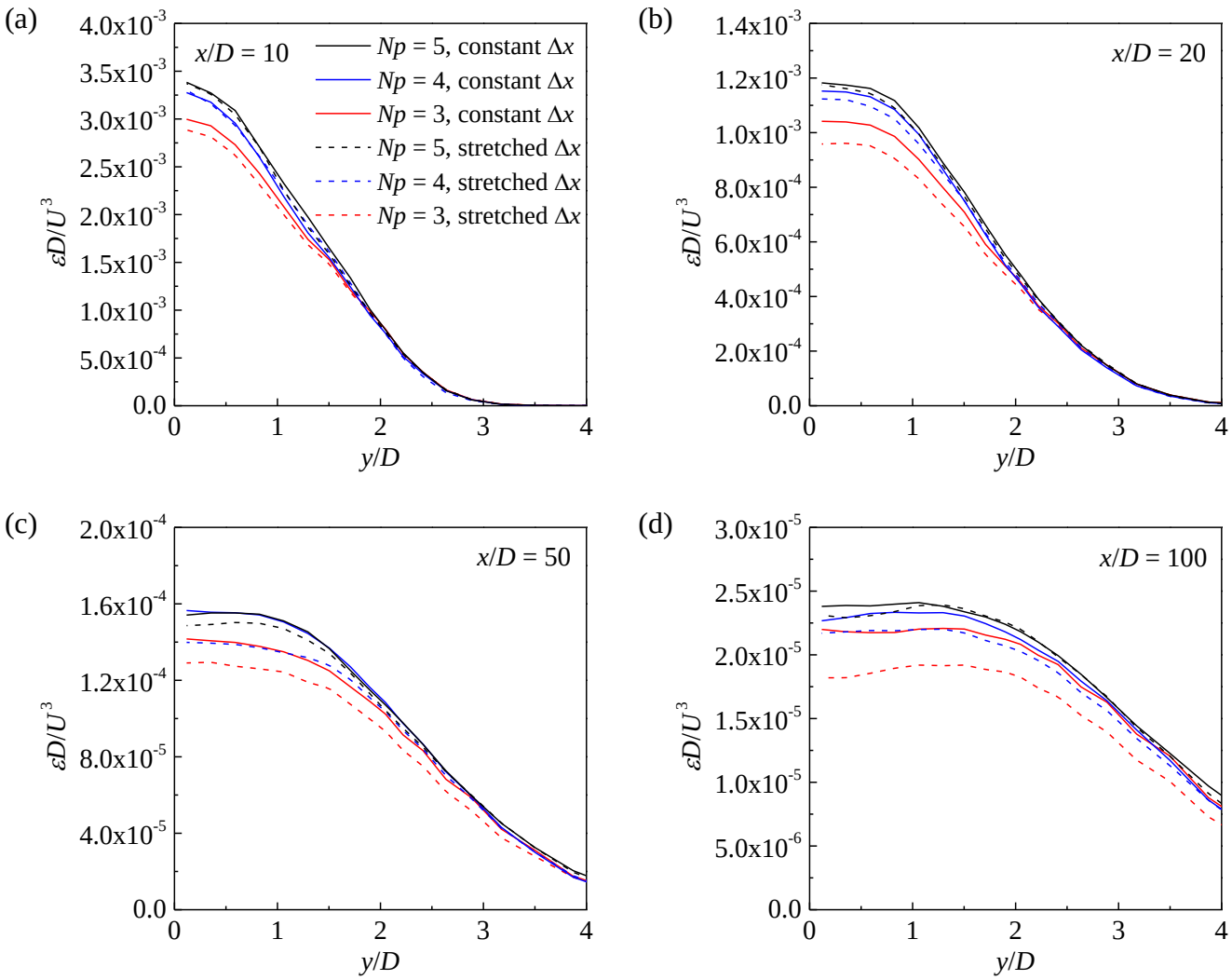

Fig. 26. Transverse distribution of the mean kinetic energy dissipation rate at (a) x/D = 10, (b) x/D = 20, (c) x/D = 50, and (d) x/D = 100.

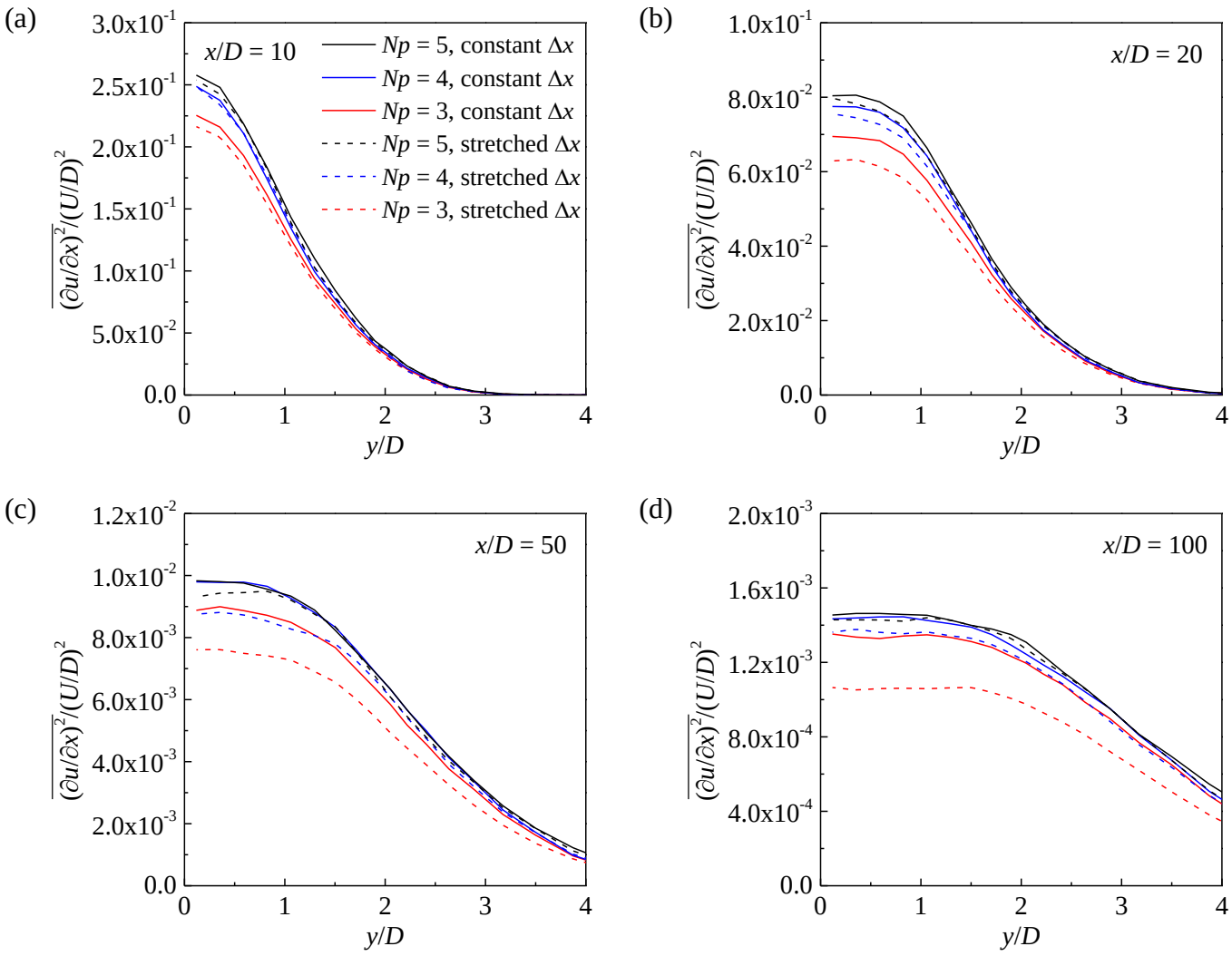

Fig. 27. Transverse distribution of the term $\overline{(\partial u/\partial x)^2}$ at (a) x/D = 10, (b) x/D = 20, (c) x/D = 50, and (d) x/D = 100.

Thirdly, the adequacy of the statistical time period (= 100T) and sample interval (= T/16) for the mean dissipation rate obtained in Fig. 26 was examined. The vortex shedding period T (which may vary from period to period) was determined based on the time history of C_L. Based on the reference case, the adequacy of the statistical time period was examined by calculating the dissipation rate using another 100T of statistical period, while the adequacy of the sample interval was examined by calculating the dissipation rate using a doubled sample interval of T/8. Fig. 28 shows the transverse distribution of the dissipation rate for the reference case and two variation cases, which suggested that the statistical time period and sample interval used for the reference case (i.e. 100T and T/16, respectively) were adequate. Similar convergence performance was also observed for the velocity derivative terms, e.g. the terms $2\overline{(\partial u/\partial x)^2}$, $\overline{(\partial v/\partial x)^2}$ and $\overline{(\partial w/\partial x)^2}$ illustrated in Fig. 29.

In addition, we also tested a case where the vortex shedding period T (and the

sampled time instants) was determined based on the time history of v sampled at (x/D, y/D, z/D) = (10, 1, 3), such that T may be different from that determined from the time history of C_L, and the flow fields used to calculate the dissipation rate were at different time instants. Nevertheless, the transverse distribution of the mean kinetic energy dissipation rate predicted by the two cases displayed negligible difference (omitted for brevity).

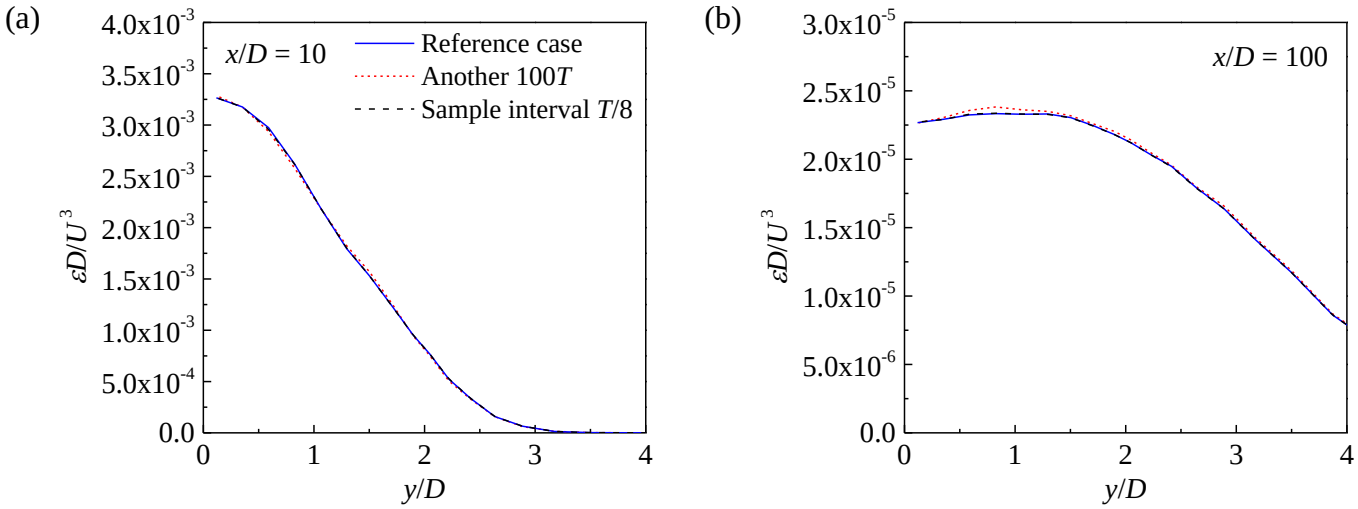

Fig. 28. Transverse distribution of the mean kinetic energy dissipation rate at (a) x/D = 10 and (b) x/D = 100, based on different statistical time periods and sample intervals.

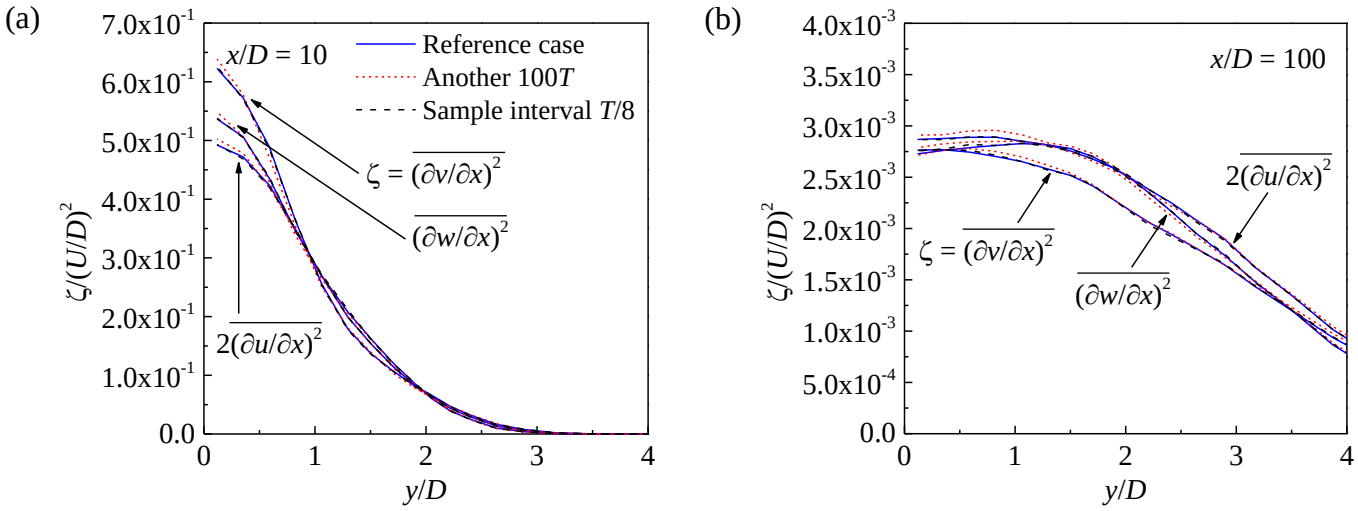

Fig. 29. Transverse distribution of several velocity derivative terms at (a) x/D = 10 and (b) x/D = 100, based on different statistical time periods and sample intervals.

Fourthly, the influence of the SVV and time integration techniques was examined. Based on the reference case, the influence of the SVV technique was examined by a variation case where the artificial diffusion induced by the SVV technique was reduced by half (through reducing the SVV diffusion coefficient from 0.1 to 0.05), while the influence of the time integration technique was examined by a case where

the time-step size was reduced by half (from 0.003125 to 0.0015625). Fig. 30 shows the transverse distribution of the dissipation rate for the reference case and two variation cases, which suggested that the SVV diffusion and time-step size did not induce noticeable influence on the prediction of the dissipation rate.

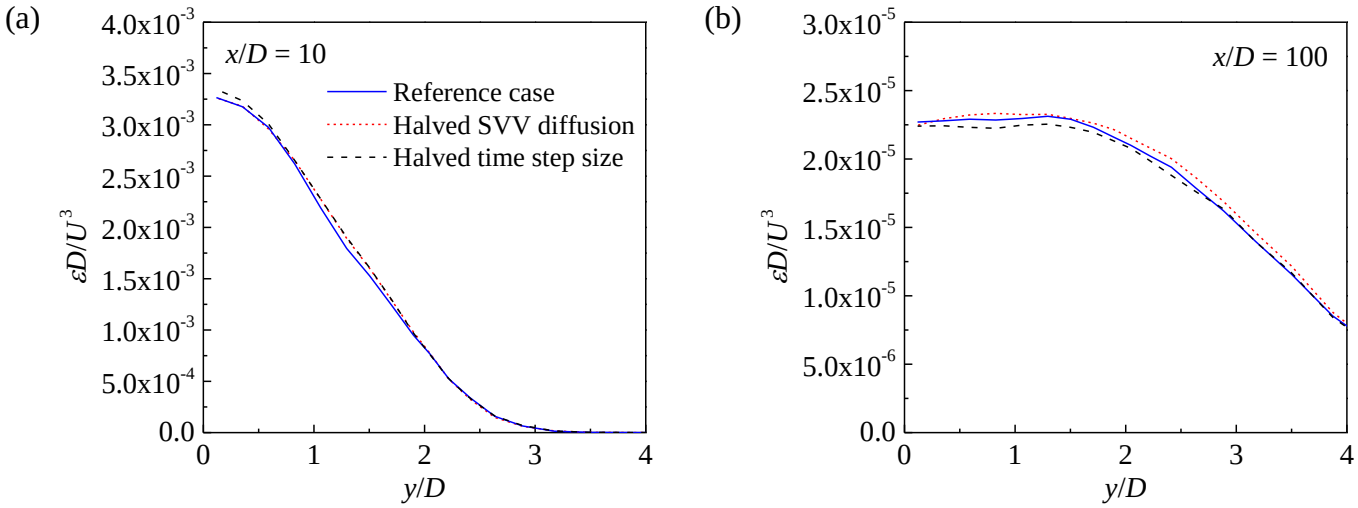

Fig. 30. Transverse distribution of the mean kinetic energy dissipation rate at (a) x/D = 10 and (b) x/D = 100, based on different SVV diffusion coefficients and time-step sizes.

After the mesh and parameter dependence studies on the mean dissipation rate ε, the Kolmogorov length scales η in the wake can be readily determined as

$$\eta = \left(\frac{\nu^3}{\varepsilon} \right)^{1/4}, \tag{B.6}$$

where ε was predicted by the reference mesh and a statistical period of 200T, and no surrogate was used. The ε profiles shown in Fig. 26 indicated that the maximum ε occurred along the wake centreline, which indicated that the minimum η (which required highest mesh resolution) occurred along the wake centreline. Therefore, the variation of η along the wake centreline is plotted in Fig. 31(a). Fig. 31(a) also shows the experimental results of Chen et al. (2018) obtained at Re = 2500. Since η/D scales with $Re^{-3/4}$ (Pope, 2000), the experimental results for Re = 2500 were transformed to those for Re = 1000 based on

$$\left(\frac{\eta}{D} \right)_{Re=1000} = \left(\frac{1000}{2500} \right)^{-3/4} \times \left(\frac{\eta}{D} \right)_{Re=2500}. \tag{B.7}$$

As shown in Fig. 31(a), the two sets of data displayed a qualitative agreement. Quantitatively, the experimental results by Chen et al. (2018) were 17%, 10% and 8% larger than the present results for x/D = 10, 20 and 40, respectively. This may be largely related to an underestimate of the dissipation rate in Chen et al. (2018) by 46%, 30% and 18% for x/D = 10, 20 and 40, respectively (based on the error propagation analysed by Zhou et al. (2003)), which, according to equation (B. 6), translated to an

overestimate of η by 16%, 9% and 5% for x/D = 10, 20 and 40, respectively. Fig. 31(b) shows the ratio between the cell size in the streamwise direction ($\Delta x/N_p$) and the Kolmogorov length scale η. Over the majority of the wake region, the ratio was close to unity.

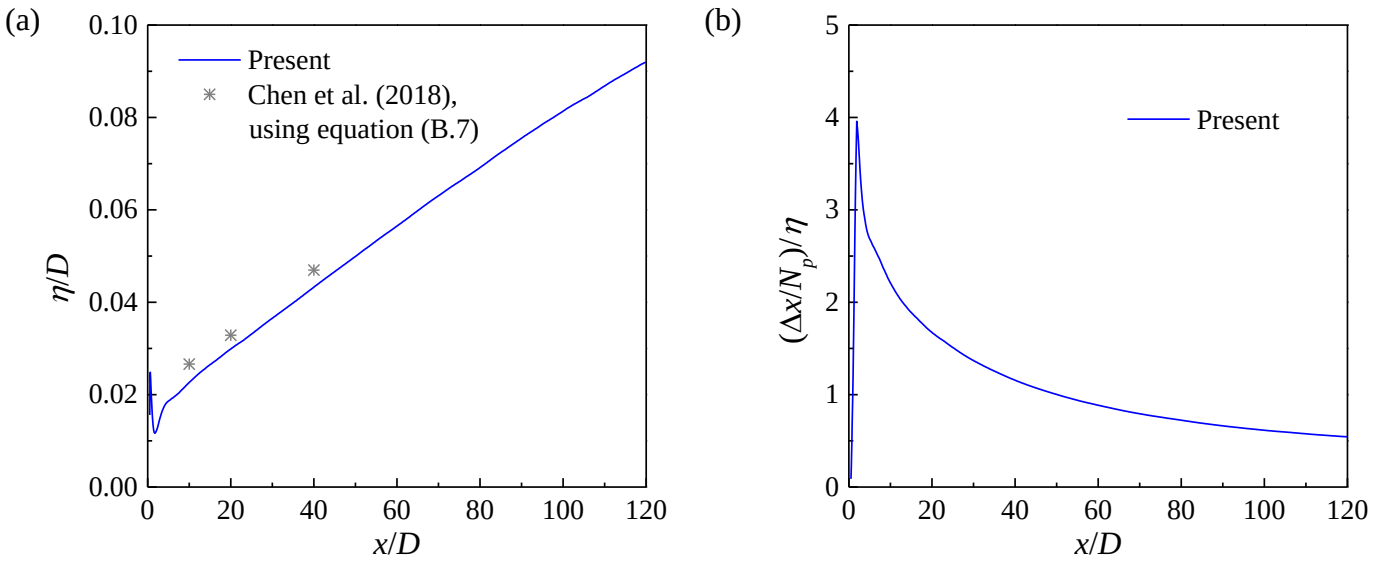

Fig. 31. Kolmogorov length scale for Re = 1000: (a) variation of η/D along the wake centreline, and (b) ratio between the cell size in the streamwise direction ($\Delta x/N_p$) and the Kolmogorov length scale η.

To further affirm the adequacy of the resolution for the small-scale turbulence, Kolmogorov-scale normalised spectra of u' obtained at several locations in the cylinder wake are presented in Fig. 32. Specifically, after obtaining a frequency spectrum in a similar manner to that introduced in section 3.2, the frequency f and energy A^2 are then normalised by the Kolmogorov scales as

$$k_1^* = \frac{f}{f_K}, \tag{B.8}$$

$$\int_0^\infty E_{11}^*\left(k_1^*\right)\mathrm{d}k_1^* = \left(u^*\right)^2 = \left(\frac{\overline{u'}}{u_K}\right)^2, \tag{B.9}$$

where the Kolmogorov frequency and velocity scales are defined as

$$f_K = \frac{\bar{u}}{2\pi\eta}, \tag{B.10}$$

$$u_K = \frac{\nu}{\eta}, \tag{B.11}$$

and $E_{11}^*\left(k_1^*\right)$ represents the spectral density. For various turbulent flows (e.g. cylinder wake, boundary layer flow, grid turbulence, etc.) and over a wide range of

Taylor microscale Reynolds numbers (Re_λ) beyond a threshold of 20 to 30, a collapse of the dissipation range of the normalised spectra (i.e. $k_1^* \gtrsim 10^{-1}$) is observed (Saddoughi and Veeravalli, 1994; Chassaing, 2000; Antonia et al., 2014). The Taylor microscale Reynolds number is defined as

$$Re_\lambda = \frac{\overline{u'}\lambda}{\nu}, \tag{B.12}$$

where

$$\lambda = \overline{u'}\sqrt{15\frac{\nu}{\varepsilon}}. \tag{B.13}$$

As shown in Fig. 32, the present dissipation ranges collapsed well with that measured by Tang et al. (2016) in the far wake of a circular cylinder, that measured by Antonia et al. (1998) in the wake of a grid plane, and that summarised by Chassaing (2000) based on various turbulent flows.

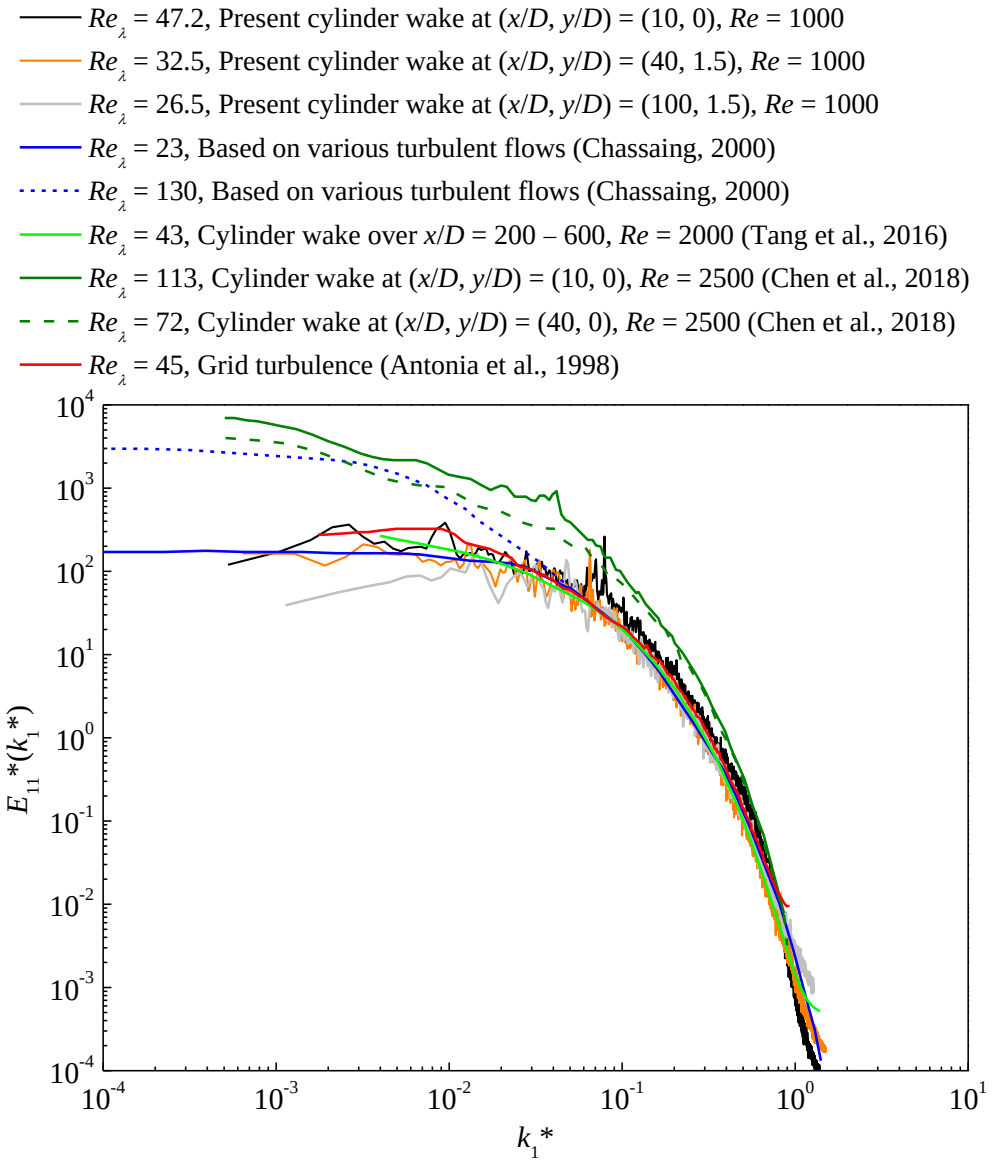

Fig. 32. Kolmogorov-scale normalised spectra of u'.

Appendix C. Numerical convergence of the frequency spectra of v

A convergence check of the frequency spectra of v obtained in section 3.2 is reported below. A particular focus lay in an accurate determination of the x/D value for the disappearance of the frequency peak at St. Based on the reference case with the time histories of v sampled at y/D = 1.5, three variation cases were tested.

(i) Case 1. The adequacy of the statistical time period for the time history of v was examined by reducing the time period from 100T to 50T.

(ii) Case 2. The adequacy of the sample interval for the time history of v was examined by increasing the sample interval from 6Δt* to 12Δt*.

(iii) Case 3. The adequacy of the number of frequency spectra sampled at a fixed (x, y) and different spanwise locations for the average of the frequency spectra was examined by reducing the equally-spaced spanwise locations from 16 to 8.

Fig. 33 shows the streamwise variation of the amplitude of v at St determined by the reference case and the three variation cases. Compared with the reference case, variation cases 2 and 3 did not show any noticeable difference, while case 1 showed a slight difference over x/D = 40–60. Nevertheless, the x/D value for the disappearance of the frequency peak at St, as determined by a comparison between the amplitude at St and the noise level, agreed well with that determined from the reference case. Specifically, the reference case obtained x/D = 49.1, while the three variation cases obtained x/D = 49.8, 49.1 and 49.4, respectively.

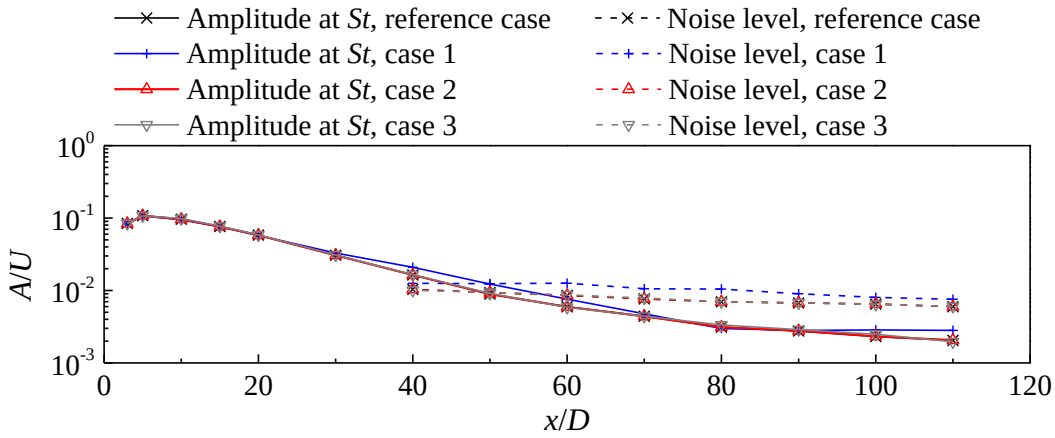

Fig. 33. Streamwise variation of the amplitude of v at St for the time histories of v sampled at y/D = 1.5.

References

Antonia, R.A., Djenidi, L., Danaila, L., 2014. Collapse of the turbulent dissipative range on Kolmogorov scales. Physics of Fluids 26, 045105.

Antonia, R.A., Zhou, T., Zhu, Y., 1998. Three-component vorticity measurements in a turbulent

grid flow. Journal of Fluid Mechanics 374, 29–57.

Browne, L.W.B., Antonia, R.A., Shah, D.A., 1987. Turbulent energy dissipation in a wake. Journal of Fluid Mechanics 179, 307–326.

Browne, L.W.B., Antonia, R.A., Shah, D.A., 1989. On the origin of the organised motion in the turbulent far-wake of a cylinder. Experiments in Fluids 7, 475–480.

Cantwell, C.D., et al., 2015. Nektar++: An open-source spectral/hp element framework. Computer Physics Communications 192, 205–219.

Cantwell, B., Coles, D., 1983. An experimental study of entrainment and transport in the turbulent near wake of a circular cylinder. Journal of Fluid Mechanics 136, 321–374.

Chassaing, P., 2000. Turbulence en m ́ecanique des fluids.

Cimbala, J.M., Nagib, H.M., Roshko, A., 1988. Large structure in the far wakes of two-dimensional bluff bodies. Journal of Fluid Mechanics 190, 265–298.

Chen, J.G., Zhou, Y., Zhou, T.M., Antonia, R.A., 2016. Three-dimensional vorticity, momentum and heat transport in a turbulent cylinder wake. Journal of Fluid Mechanics 809, 135–167.

Chen, J.G., Zhou, Y., Antonia, R.A., Zhou, T.M., 2018. Characteristics of the turbulent energy dissipation rate in a cylinder wake. Journal of Fluid Mechanics 835, 271–300.

Ducci, A., Konstantinidis, E., Balabani, S., Yianneskis, M., 2005. Single- and two-point LDA measurements in the turbulent near wake of a circular cylinder. Engineering Turbulence Modelling and Experiments 6: Procedings of the ERCOFTAC International Symposium on Engineering Turbulence Modelling and Measurements; ETMM6, Sardinia, Italy, 451–460.

Elsner, J.W., Elsner, W., 1996. On the measurement of turbulence energy dissipation. Measurement Science and Technology 7, 1334–1348.

George, W.K., Hussein, H.J., 1991. Locally axisymmetric turbulence. Journal of Fluid Mechanics 233, 1–23.

Hussain, A.K.M.F., Hayakawa, M., 1987. Eduction of large-scale organized structures in a turbulent plane wake. Journal of Fluid Mechanics 180, 193–229.

Jiang, H., Cheng, L., 2017. Strouhal–Reynolds number relationship for flow past a circular cylinder. Journal of Fluid Mechanics 832, 170–188.

Jiang, H., Cheng, L., 2019. Transition to the secondary vortex street in the wake of a circular cylinder. Journal of Fluid Mechanics 867, 691–722.

Jiang, H., Cheng, L., 2021. Large-eddy simulation of flow past a circular cylinder for Reynolds numbers 400 to 3900. Physics of Fluids 33, 034119.

Karniadakis, G.E., 1990. Spectral element-Fourier methods for incompressible turbulent flows. Computer Methods in Applied Mechanics and Engineering 80, 367–380.

Karniadakis, G.E., Israeli, M., Orszag, S.A., 1991. High-order splitting methods for the incompressible Navier-Stokes equations. Journal of Computational Physics 97, 414–443.

Karniadakis, G.E., Sherwin, S.J., 2005. Spectral/hp Element Methods for CFD, Oxford University Press.

Kirby, R. M., Sherwin, S. J., 2006. Stabilisation of spectral/hp element methods through spectral vanishing viscosity: Application to fluid mechanics modelling. Computer Methods in Applied Mechanics and Engineering 195, 3128–3144.

Lefeuvre, N., Thiesset, F., Djenidi, L., Antonia, R. A., 2014. Statistics of the turbulent kinetic energy dissipation rate and its surrogates in a square cylinder wake flow. Physics of Fluids 26, 095104.

Matsumura, M., Antonia, R. A., 1993 Momentum and heat transport in the turbulent intermediate wake of a circular cylinder. Journal of Fluid Mechanics 250, 651–668.

Moxey, D., et al., 2020. Nektar++: Enhancing the capability and application of high-fidelity spectral/hp element methods. Computer Physics Communications 249, 107110.

Noca, F., Park, H., Gharib, M., 1998. Vortex formation length of a circular cylinder (300 < *Re* < 4000) using DPIV. Proceedings on Bluff Body Wakes and Vortex-Induced Vibration, ASME Fluids Engineering Division.

Norberg, C., 1994. An experimental investigation of the flow around a circular cylinder: influence of aspect ratio. Journal of Fluid Mechanics 258, 287–316.

Norberg, C., 2003. Fluctuating lift on a circular cylinder: review and new measurements. Journal of Fluids and Structures 17, 57–96.

Pope, S.B., 2000. Turbulent Flows. *Cambridge University Press*. p186.

Reynolds, W.C., Hussain, A. K. M. F., 1972. The mechanics of an organized wave in turbulent shear flow. Part 3. Theoretical models and comparisons with experiments. Journal of Fluid Mechanics 54, 263–288.

Roshko, A., 1954. On the development of turbulent wakes from vortex streets. NACA report 1191.

Saddoughi, S.G., Veeravalli, S.V., 1994. Local isotropy in turbulent boundary layers at high Reynolds number. Journal of Fluid Mechanics 268, 333–372.

Tang, S.L., Antonia, R.A., Djenidi, L., Zhou, Y., 2016. Complete self-preservation along the axis of a circular cylinder far wake. Journal of Fluid Mechanics 786, 253–274.

Taylor, G.I., 1935. Statistical theory of turbulence. Proceedings of the Royal Society A: Mathematical, Physical and Engineering Sciences 151, 421–444.

Wieselsberger, C., 1922. New data on the laws of fluid resistance. NACA Technical Note 84. National Advisory Committee for Aeronautics, Washington, DC, United States.

Williamson, C.H.K., 1996. Vortex dynamics in the cylinder wake. *Annual Review of Fluid Mechanics* 28, 477–539.

Williamson, C.H.K., Roshko, A., 1990. Measurements of base pressure in the wake of a cylinder at low Reynolds numbers. Zeitschrift fuer Flugwissenschaften und Weltraumforschung 14, 38–46.

Williamson, C.H.K., Prasad, A., 1993. A new mechanism for oblique wave resonance in the 'natural' far wake. Journal of Fluid Mechanics 256, 269–313.

Zdravkovich, M.M., 1997. Flow around circular cylinders, Volume 1: Fundamentals. *Oxford University Press*.

Zhang, H.J., Zhou, Y., Antonia, R.A., 2000. Longitudinal and spanwise vortical structures in a turbulent near wake. Physics of Fluids 12, 2954–2964.

Zhou, T., Zhou, Y., Yiu, M.W., Chua, L.P., 2003. Three-dimensional vorticity in a turbulent cylinder wake. Experiments in Fluids 35, 459–471.

Zhou, T., Antonia, R.A., 2000. Reynolds number dependence of the small-scale structure of grid turbulence. Journal of Fluid Mechanics 406, 81–107.

Zhou, Y., Zhang, H.J., Yiu, M.W., 2002. The turbulent wake of two side-by-side circular cylinders. Journal of Fluid Mechanics 458, 303–332.

Zhu, Y., Antonia, R.A., 1997. On the correlation between enstrophy and energy dissipation rate in a turbulent wake. Applied Scientific Research 57, 337–347.